Optimized NiFeP alloy for overall water-splitting

Sonia Carbone [a], Roberto Luigi Oliveri [a], Bernardo Patella [a], Giuseppe Aiello [a],
Michelangelo Scopelliti [b,c], Nicola Campagna [a], Filippo Pellitteri [a], Rosario Miceli [a],
Alberto Affranchi [d], Sonia Longo [a], Maurizio Cellura [a,d], Philippe Mandin [e], Myeongsub Kim [f],
Rosalinda Inguanta [a,*]

[a] Dipartimento di Ingegneria, Università degli Studi di Palermo, Viale delle Scienze, 90128, Palermo, Italy
[b] Dipartimento di Fisica e Chimica – Emilio Segrè, Università degli Studi di Palermo, Viale delle Scienze 17, 90128, Palermo, Italy
[c] Laboratorio Superfici, Film Sottili e Dispositivi, ATEN Center, Università degli Studi di Palermo, Viale delle Scienze 18/A, 90128, Palermo, Italy
[d] Centro di Sostenibilità e Transizione Ecologica, Università degli Studi di Palermo, Viale delle Scienze, 90128, Palermo, Italy
[e] Université de Bretagne Sud, IRDL UMR CNRS 6027, Lorient, France
[f] Ocean and Mechanical Engineering, Florida Atlantic University, 777 Glades Rd., Boca Raton, FL, 33431, United States

ARTICLE INFO

ABSTRACT

To achieve efficient electrochemical processes for the hydrogen evolution reaction (HER) and oxygen evolution reaction (OER), it is essential to develop rational designs and innovative modifications to low-cost, high-performance electrocatalysts able to work in direct connection with renewable sources. This paper presents the behavior of nanostructured NiFeP electrocatalysts to use for both HER and OER. The electrodes consist of nanowire arrays with a large surface area, ensuring high electrocatalytic activity. The most promising results were obtained for the OER, with a Tafel slope of 40 mV/dec. Electrodes demonstrate good stability over time without any evident signs of performance decay. Also, in the case of operation under intermittent power supply, applying current profiles typical of a day-night cycle of photovoltaic and wind energy, good performance was obtained. A lab-scale electrolyzer was fabricated and tested for a continuous operation of 6 h at 50 and 100 mA/cm^2, reaching a potential of 1.91 and 2.01 V, respectively, for overall water-spitting. Furthermore, the environmental impact of the manufacturing process of NiFeP nanowires was evaluated by applying the Life Cycle Assessment methodology, which is employed to assess the energy and environmental impacts of the life cycle of electrodes produced by the electrodeposition method.

1. Introduction

Significant progress has been made in lowering the costs of renewable energy sources (RESs), including wind and solar photovoltaic (PV) systems. Their intermittent nature necessitates local energy storage to maintain a balance between energy supply and demand [1]. Therefore, developing technologies to convert renewable solar and wind energy into non-electrical energy storage is essential to maximize its benefits. Clean hydrogen emerges as a leading solution for seasonal flexibility, supporting congestion management and balancing renewable energy variability [2]. Hydrogen can be generated from electricity as needed, stored for several months, transported through pipelines, and used as a chemical feedstock [3]. Hydrogen is used in various industrial applications such as chemical production, refining, metallurgy, and glass and electronics manufacturing. Today, hydrogen is typically produced by methane steam reforming, which results in carbon dioxide emissions and contributes to global climate change. Electrochemical hydrogen production using electrolyzers offers a practical solution to produce green-H$_2$ [4] and utilize the excess electricity generated from renewable energy sources [5]. In renewable power-to-hydrogen (P2H) systems, power electronics play a crucial role in supplying electrolyzers using different possible topologies of electrical power converters, providing high DC currents, and avoiding accelerated degradation [6].

The main drawback of green hydrogen is the high production cost, although many literature reviews predict that the production cost will decrease due to technological advances in hydrogen technology [7]. The main challenge of electrolyzer technology is the energy required to activate the water-splitting reaction [8]. Electrode overpotential

---

* Corresponding author.
  E-mail address: rosalinda.inguanta@unipa.it (R. Inguanta).

accounts for the most significant energy losses [9], which largely depend on the types of electrodes and electrocatalysts [10]. Therefore, there is a growing need for active, stable, and low-cost electrocatalysts for efficient hydrogen [11] and oxygen [12] production from water splitting. The focus is in particular on the development of stable electrocatalysts even at high current densities and for long operating times to bridge the gap between laboratory-scale research and real industrial application [13].

Polymer electrolyte membrane electrolyzer (PEME) outperforms alkaline electrolyzer (AE) in terms of hydrogen production for the same energy consumption [14]. Nevertheless, the use of noble metals such as Pt or IrO_2 as PEME electrocatalysts makes the cost of these devices exorbitant, primarily for large-scale systems [15]. On the contrary, AE requires less noble electrocatalysts owing to the more beneficial kinetic conditions [16].

Due to their corrosion resistance and good electrocatalytic properties in alkaline solutions, Ni-based materials are frequently used as electrocatalysts in AE [17]. Ni alloys are ideal as HER catalysts as they inhibit the formation of hydrides, which can deactivate the catalyst surface [18]. The most effective Ni alloys include NiPt [19], NiMo [20], NiZn [21], NiCo [22], NiCoCr [23] and NiFe. In particular, the binary Ni-Fe alloy has been extensively studied because promising bifunctional catalyst for water splitting [24], even with alternative compositions such as nitrides, phosphides, sulfides, and borides [25,26]. Transition metal phosphides (TMPs) have recently emerged as a new class of catalysts that, due to their unique properties, can catalyze OER more efficiently than conventional oxide- or hydroxide-based catalysts (partially positive and partially negative charges in the metal and phosphorus, respectively) [27,28]. The exploration of TMPs is a rapidly growing area in developing electrocatalysts with high catalytic activity and stability in both acidic and basic conditions [29], even if achieving electrocatalysts with at least three elements is a considerable challenge. Zhao et al. [30] have performed a systematic study on crystalline $(Ni_{1-x}Fe_x)_3P$, finding excellent activity (overpotential of 233 mV at 10 mA/cm^2) and enhanced stability during a 120 h potentiostatic test. Amorphous NiFe phosphatized alloys with different concentrations of phosphorus, obtained by one-step electrodeposition on Ni foam by Xu et al. [31], were used as bifunctional electrocatalysts in an alkaline solution. A cell potential of 1.59V at 10 mA/cm^2 was measured, less than that of NiFe (1.83V). The excellent performance of phosphatized alloy was attributed to the high active site number due to the amorphous structure. Similar results (cell potential of 1.63V at 10 mA/cm^2) were also obtained by Zhang et al. using NiFeP bifunctional electrocatalysts fabricated through a melting method and post-phosphorization treatment [32]. Interesting results were also obtained by Calderon et al. [33], who tested the quaternary alloy NiFePZn, obtained by co-electrodeposition on AISI 304 steel. The alloy shows, in 1 M NaOH at 10 mA/cm^2, overpotentials of 163 mV and 262 mV for HER and OER, respectively, while for overall water splitting, a cell potential equal to 1.65 V (at 10 mA/cm^2) was measured. Different explanations can be found in the literature regarding the effect of the presence of phosphorus atoms on alloy performance. For Liu and Rodriguez [34], who have analyzed the electrocatalysts using density functional theory, phosphorus atoms dilute the concentration of highly active nickel sites, resulting in moderate binding to the intermediates and products, known as the 'ensemble effect'. Zhang et al. [35], analyzing the $NiCo_2P_x$ catalyst for HER, attributed the excellent performance (high electrocatalytic activity and long-term durability and stability in different electrolytes at different pH) to the presence of phosphorus in the catalytic system, which further weakened the H-OH bond facilitating the dissociation of water.

In this study, two strategies were used to improve the electrocatalytic activity: modulating the alloy composition to obtain a ternary alloy in a single step and selecting a fabrication process that results in a nanostructured morphology. As reported in the literature [36], nanostructured morphology is another critical issue in improving electrochemical performance with more exposed active sites. The

unique properties of one-dimensional nanomaterials, including their high specific surface area and increased edge-to-face ratio, have significantly improved the electrochemical performance of the alloy [36]. Indeed, the significant surface-to-volume ratio of nanostructures provides substantial electrochemical surface areas with numerous active sites that are readily accessible to the electrolyte. This feature ensures superior electrocatalytic activity per electrode area and/or mass of the material. In addition, carrier transport paths are hastened and shortened in a nanostructured electrode, thereby facilitating the kinetics of the electrochemical reaction.

NiFeP nanowires were obtained by the template electrodeposition method [37] following the previously obtained results [38]. Template electrosynthesis was selected as the fabrication method because it is a cost-effective approach, significantly reducing the materials required for the synthesis process [39]. This method requires only small volumes of solutions, typically aqueous, short synthesis times, and low energy consumption.

In this work, the performance of NiFeP alloy nanowires for both HER and OER was explored in alkaline conditions. Tests were also perfomed in an alkaline solution containing NaCl to simulate the seawater composition. The electrodes were subjected to several electrochemical and morphological characterization techniques to assess any variations in morphology and composition. The NiFeP ternary alloy, especially with nanowire morphology, is little investigated in comparison to the binary alloy. In addition, up to today, the properties for times not exceeding 24 h were explored, and the study was limited either to the HER reaction only or to that of OER. Here, the stability of the electrodes was assessed over 125 h of operation under constant current. In addition, their ability to operate under intermittent power supply, typical of renewable energy supply, was demonstrated. The overall water-splitting performance was evaluated using a lab-scale electrolyzer in a 30 % KOH aqueous solution at 25 °C. The alkaline electrolyzer needs only a low cell voltage of 1.68 V to achieve the current density of 10 mA/cm^2 when using NWs Ni-Fe-P as the catalyst for HER and OER. Finally, for the first time, a Life Cycle Assessment (LCA) was also carried out to assess the environmental impact of electrode production.

2. Materials and methods

This work focuses on the fabrication of nanostructured NiFeP electrodes to improve the already-known performance of NiFe nanowires (NWs) obtained in our previous works [38,40]. The electrodes were prepared by template electrosynthesis using a nanoporous polycarbonate membrane. This method, described in detail in Ref. [41], is a multi-step process where, in the first step, a thin gold film is sputtered onto one side of the template to make it conductive. The sputtering deposition was carried out using Scancoat Six Sputter Coater from Edwards Ltd by applying a continuous current of 30 mA for 3 min to obtain a gold film about 30 nm thick. The subsequent stage entails the potentiostatic electrodeposition (at −1.15 V vs. saturated calomel electrode (SCE) for 1.5 h) of a thick Ni layer (about 12 μm thick) that was deposited on the gold-coated surface of the template. This is a key step because the Ni layer confers mechanical stability, ensuring the connection of all nanowires, and acts as the current collector. A typical three-electrode cell setup was used, with platinum mesh as the counter electrode, a SCE as the reference, and the gold-coated membrane as the working electrode. The electrodeposition solution for Ni current collector is the typical Watt's bath (300 g/L $NiSO_4 \cdot 6H_2O$, 45 g/L $NiCl_2 \cdot 6H_2O$, 45 g/L H_3BO_3) at room temperature. In the final step, NiFeP alloy was deposited inside the pores of the other membrane surface by pulsed electrodeposition technique, where the voltage transitions between −1.2 V (for 6 s) and −0.75 V (for 4 s) vs. SCE for a total of 70 cycles. The appropriate parameters were derived from reference [42] and subsequently fine-tuned. Precise operating parameters are critical to obtain homogeneous nanowires with the desired elements. The deposition process takes place at −1.2 V, and subsequently, the deposit

partially dissolves during the step at −0.75 V [43]. At this potential, the current density becomes positive, allowing the composition and morphology of the nanostructure to be regulated whilst preventing the formation of gas bubbles [41]. For the synthesis of NiFeP NWs, the starting electrodeposition bath comprises Watt's solution and 0.44 M $FeSO_4 \bullet 7H_2O$ [38]. With this solution, it is possible to obtain NWs with an optimal Fe composition of approximately 78 %. The concentrations of the phosphorus precursor, $NaH_2PO_2 \cdot H_2O$, were modified to 20 g/L (referred to as NiFeP/1), 30 g/L (referred to as NiFeP/2) and 50 g/L (referred to as NiFeP/3). Using sodium hypophosphite as a source of phosphorus [43], the deposition of metal phosphide occurs by the reactions 1 and 2

$$H_2PO_2{}^- + 2H^+ + e^- \rightarrow P + 2H_2O \tag{1}$$

$$M^{z+} + P + ze^- \rightarrow MP \tag{2}$$

After electrodeposition, electrodes were immersed in four consecutive baths of pure $CHCl_3$, each lasting 5 min, to dissolve the polycarbonate membrane and obtain an array of the nanowires firmly attached to the current collector. The obtained electrode has a geometric area of about 11 cm^2 and has been cut into several pieces with a diameter of 12 mm, on which the different characterizations were performed. NWs electrodepositions were carried out in a standard three-electrode cell at room temperature. A Pt mesh was used as a counter electrode, and an SCE was used as a reference.

The electrodes were first characterized by scanning electron microscopy (SEM) using a FEG-ESEM microscope (QUANTA 200 by FEI), Energy Dispersive X-ray Spectroscopy (EDS), and X-ray diffraction (XRD) using a RIGAKU X-ray diffractometer (D-MAX 25600 HK). The surface of the NWs was also characterized through X-ray photoelectron spectroscopy (XPS) using a PHI5000 VersaProbe. NiFeP electrodes were subsequently tested as both cathodes and anodes in a 30 % w/w KOH aqueous solution at room temperature and without stirring. For the electrochemical tests, only NWs were exposed to the electrolytic solution. The performance of the ternary alloy was compared with that of the binary NiFe alloy. The influence of phosphorus on the electrocatalytic performance was assessed to identify the optimum alloy composition. Tests were performed in a standard three-electrode cell, where the nanostructured electrode served as the working electrode, a nickel strip was employed as the counter-electrode, and Hg/HgO 0.1 M NaOH was used as reference. All potentials were referred to the Reversible Hydrogen Electrode (RHE) at pH 14. Cyclovoltammetry (CV), Quasi-Steady-State Polarization (QSSP), and Galvanostatic-Step Polarization were performed. Additionally, to examine the mid- and long-term stability of electrodes, galvanostatic tests were conducted at ±50 mA/cm^2. Electrochemical long-term characterization was also carried out in an alkaline KOH solution with 0.5 M NaCl to mimic seawater composition [38]. These tests were also carried out under dynamic conditions, applying current profiles typical of photovoltaic and wind energy. Using nanostructured electrodes, a lab-scale electrolyzer was also fabricated and tested.

A Solartron Multichannel Cell Test System (Mod. 1470 E) was employed to perform electrochemical characterization, and data were recorded by MultiStat Software. Each experiment was repeated at least three times.

3. Results and discussion

3.1. Fabrication and characterization

SEM was utilized to observe the morphology of NW electrodes. Fig. 1 displays various top-view images of a NiFeP/3 NWs electrode at increasing magnifications. It is important to underline that, for all obtained electrodes, the SEM images are practically identical since NW morphology is dependent only on the template shape and not on the phosphorus content.

Owing to the shape of the nano-porous template, the NWs possess a cylindrical framework, a uniform and even surface, and are evenly
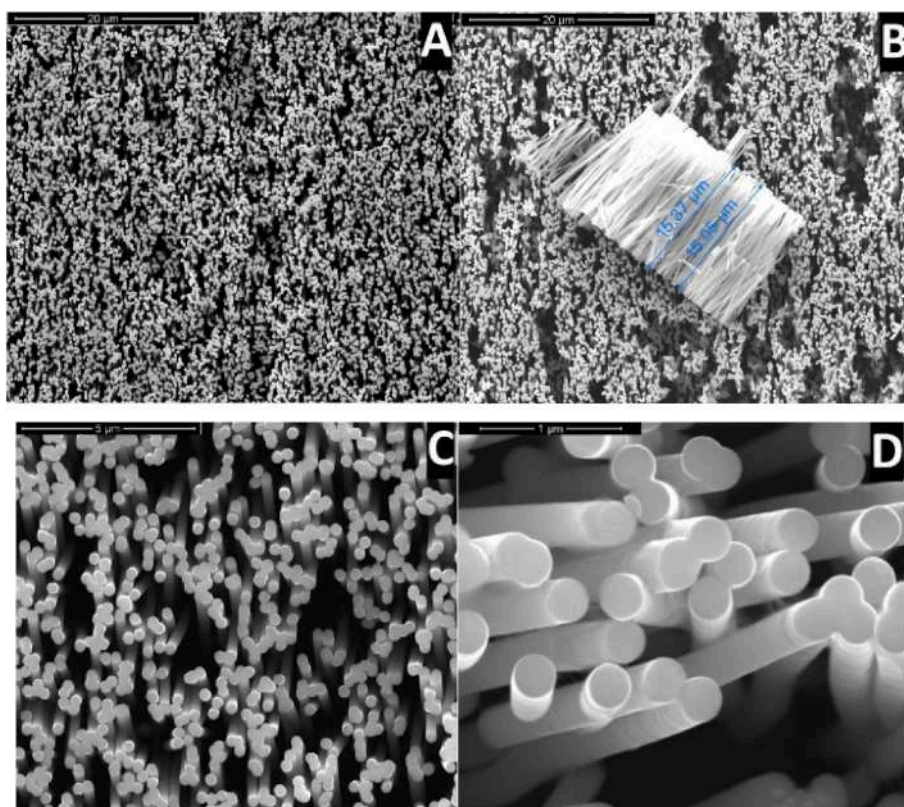

Fig. 1. SEM top-view images of NiFeP/3 NWs electrode at increasing magnification.

dispersed over the entire surface of the nickel collector, as shown in Fig. 1A. Fig. 1B displays a bundle of fallen nanowires, which allowed us to approximate their length at around 15 μm. Additionally, Fig. 1D exhibits connections between NWs due to the typical pore interconnection that characterizes polycarbonate membranes. For improved visualization of the nanostructures, SEM imaging of tilted top-view NWs has been utilized to showcase their tridimensionality (Fig. 2). The mean diameter of the NWs was about 250 nm.

EDS analysis was performed to quantify the atomic percentage of each element. To perform this analysis, the NWs were detached from the Ni collector using a copper (Cu) tape to obtain an EDS measurement with greater precision regarding the composition. Fig. 3 shows the EDS spectra of the electrodes obtained using deposition baths containing different amounts of phosphorus. For comparison, the EDS spectrum of the NiFe binary alloy is shown, highlighting the presence of Cu, which is related to the copper tape. All the elements of the ternary alloy can be observed in the other spectra. The composition of the electrodes is reported in Table 1. For comparison, the composition of binary alloy was also reported. According to the literature, NWs exhibit a higher iron content (Fe:Ni ratio is approximately 3.3) despite Ni being more noble and the solution having a higher Ni concentration, confirming the anomalous Fe deposition typical of the electrodeposition of Fe alloy [44]. Additionally, it is observed that the phosphorus content slightly rises with an increase in its concentration in the deposition bath, with a weight content ranging from 6 to 8 %.

In agreement with the literature data, the presence of phosphorus in the electrodeposition bath depresses iron deposition [33]. A non-metal, such as phosphorus, cannot be deposited in its pure form from aqueous solutions. In contrast, phosphorus can be easily deposited from aqueous solutions containing Fe group elements. The deposition of phosphorus next to Fe group metals is called "induced co-deposition". Hydrogen can also act as an inducing element, especially when the reduction of Fe group metals is also involved. The reduction of the inducing element and phosphorus are closely linked, as only one electron is available for the
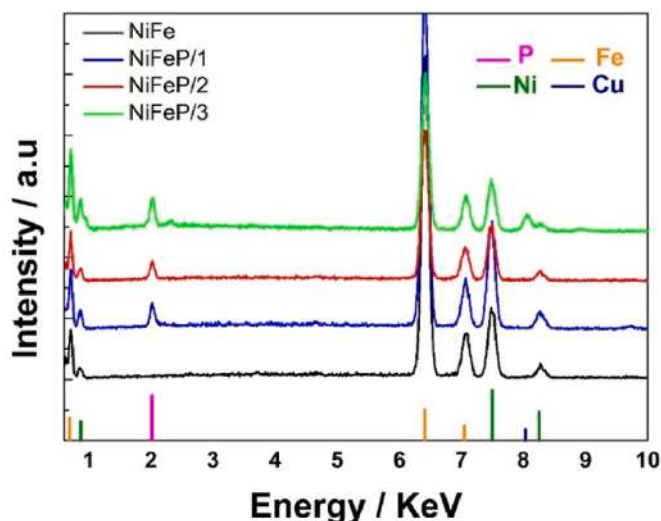

Fig. 3. EDS spectra of NiFeP NWs with different phosphorus concentrations. For comparison, the spectrum of NiFe NWs was also reported.

Table 1
Composition of NiFeP and NiFe electrodes measured throughout EDS analyses.

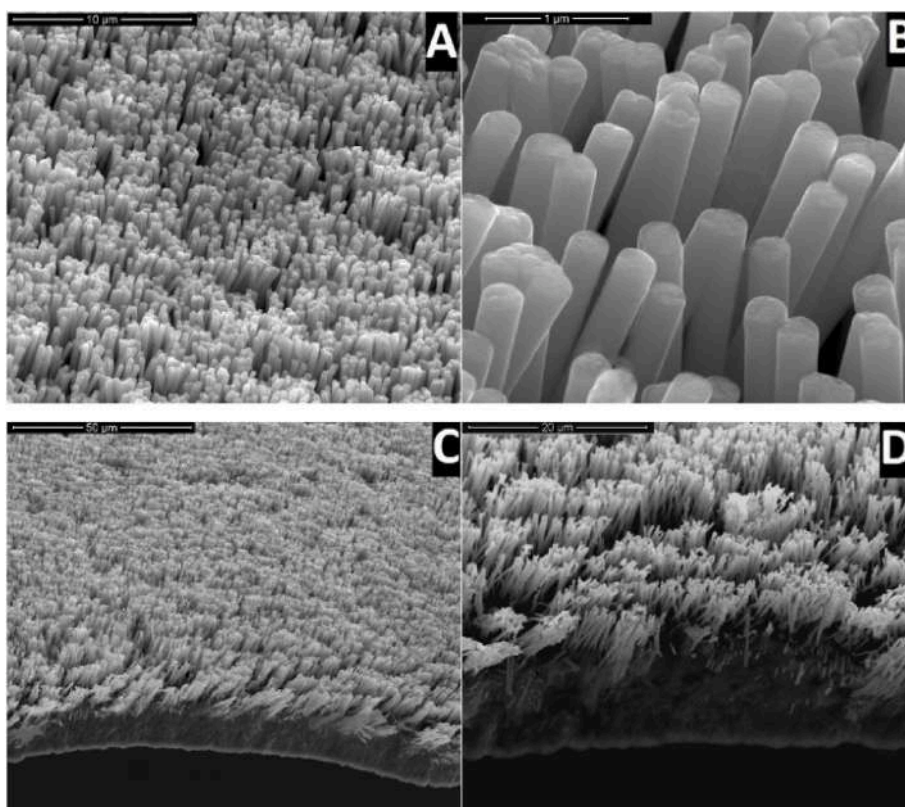|	Ni	Fe	P
NiFe	21.05	78.95	/
NiFeP/1	20.85	73.22	5.93
NiFeP/2	20.69	72.60	6.71
NiFeP/3	19.41	72.92	7.67

Fig. 2. SEM tilted top-view images of NiFeP/3 NWs electrodes at increasing magnification.

discharge of the phosphorus for every electron involved in the discharge of the inducing element. As a result, only half of the total current can be used to discharge the phosphorus [45]. This explains why the phosphorus content in the electrodes is relatively low compared to the other alloying elements, despite the increased concentration in the deposition bath.

As illustrated in Fig. 4B, the EDS analysis was also conducted to evaluate the composition variation of the three elements (Ni, Fe, P) along the NW length. In particular, the EDS line was performed on the NWs bundle of Fig. 4A. The results indicate that the composition within the NWs is homogeneous, with an almost constant trend. To further verify this result, EDS mapping was also carried out on a single NW. As can be observed in Fig. 4C, the mapping of the three elements shows a uniform distribution along the NW length.

The X-ray diffraction patterns of NiFeP NWs were reported in Fig. 5. Using the XRD database [46], the diffraction peaks present in Fig. 5A were identified. The peaks, located at 44.5°, 51.8°, 76.3°, and 92.8°, are assigned to crystalline Ni, and it can be attributed to the Ni current collector. The peaks of the NiFe alloy were detected at about 2θ of 43.5°, 50.3°, 74.1°, and 89.9°. The intensity of the peak at 2θ = 50.3° was the strongest among the three peaks. These results indicate the deposition of a crystalline alloy. This result is in agreement with the data reported in Ref. [45], wherein it was demonstrated that alloys containing approximately 7 % phosphorus are crystalline. Specifically, it was reported that alloys with about 7 % phosphorus are crystalline and exhibit a propensity to become amorphous as the phosphorus content increases. The alloys obtained in this work are all crystalline, but the decrease in the intensity of the peaks with increasing P and the shift in the 2Theta angles, visible through the main diffraction peak in Fig. 5B, is indicative of an alteration in the lattice structure of the alloy. The mean grain size of the alloy, d, was calculated from Scherrer's equation (equation (3)):

$$d = 0.94\lambda/\beta \cos\theta \qquad (3)$$

where λ is the wavelength of radiation, θ is the diffraction angle, and β is the full-width half maximum in radians of the main intensity peak.

According to Refs. [31,47], no phosphide phases are present in the diffraction pattern of all NiFeP alloys, but the phosphorus present in the structure of the alloy causes a deviation in the crystalline lattice, which also modifies the size of the grains, Fig. 5B. The mean grain size increases from about 31 ± 1.1 nm to about 40 ± 1.7 nm, passing from NiFe to NiFeP alloy. Given that the P content in the alloy varies slightly from 6 to 8 %, the mean grain size in the NiFeP alloy also varies little, in the 37–40 nm range. This analysis was done on the entire peak, although the inclusion of phosphorus in the binary alloy leads to the formation of a double peak and, therefore, to the formation of another phase. This new phase is probably the Ni_3P [48], which has a diffraction peak at 50.5°. Therefore, a more accurate grain size analysis should be done after the deconvolution of the two peaks.

The behavior of electrodes based on NiFeP was examined using various techniques. To evaluate the benefits of nanostructured morphology, both NiFeP/3 and a Nickel planar strip with the same geometric area were tested in 30 % KOH via CVs at varying scan rates. The specific capacitance was then estimated using the double-layer capacitance method [49], as it is correlated with the electrochemically active surface area. Cyclic voltammetry was performed in a non-Faradaic region, ranging from 0.64 to 0.74 V vs. RHE, where no reactions occurred. The inset of Fig. 6 depicts the CVs of NiFeP NWs. For each scanning rate, the difference between anodic and cathodic current density at 0.7 V vs. RHE was computed and then plotted against the scan rate. The slope of the linear fit is the double-layer capacitance. The slope of NiFeP/3 is much greater than that of the Ni planar strip. This is a good result due to the very large surface area of the NWs. This attribute is expected to enhance the electrocatalytic performance. The slope value of NiFeP is consistent with the literature [50] and is plausible because it is in good agreement with the value calculated from the analysis of SEM images using the equation proposed in Ref. [51].

QSSP tests were carried out for both HER and OER. A range of 0.7 V has been analyzed with a scan rate of 0.1667 mV s⁻¹, Fig. 7. From this
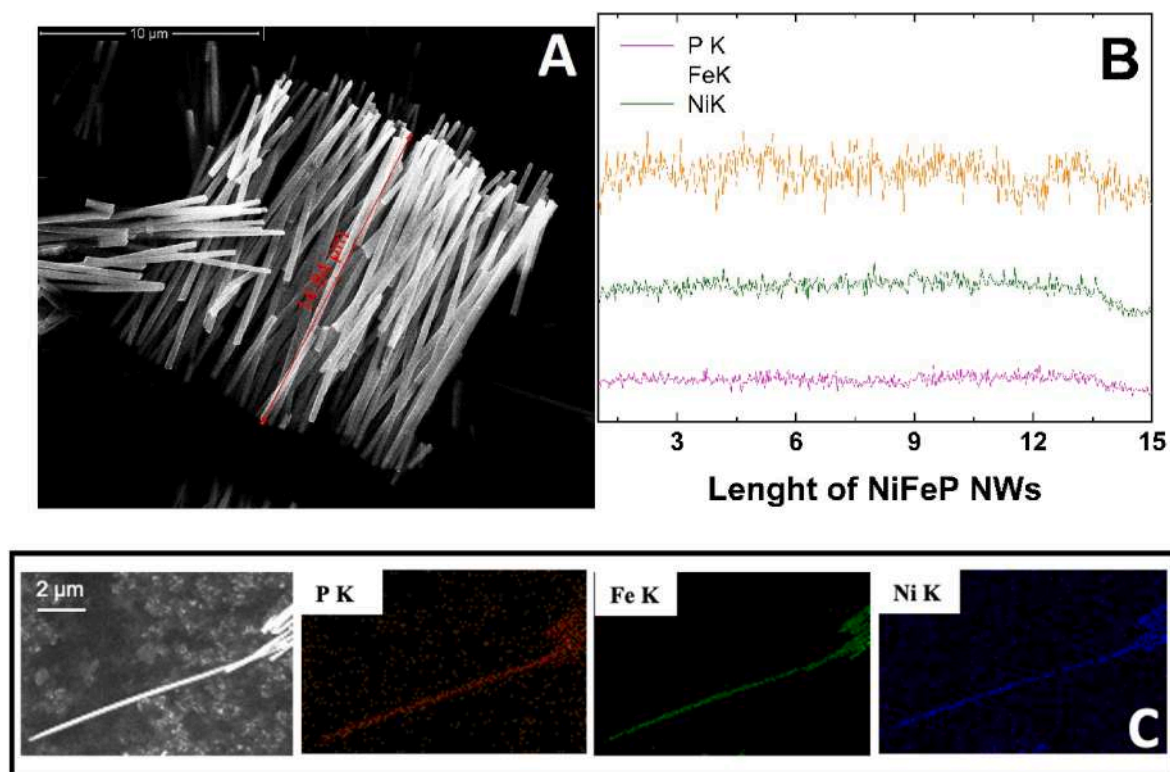

Fig. 4. A) SEM image of NiFeP/3NWs bundle detached from Ni current collector. B) EDS-line analysis performed on the bundle of Fig. 4A. C) EDS-mapping analysis performed on a single NiFeP/3 NW.
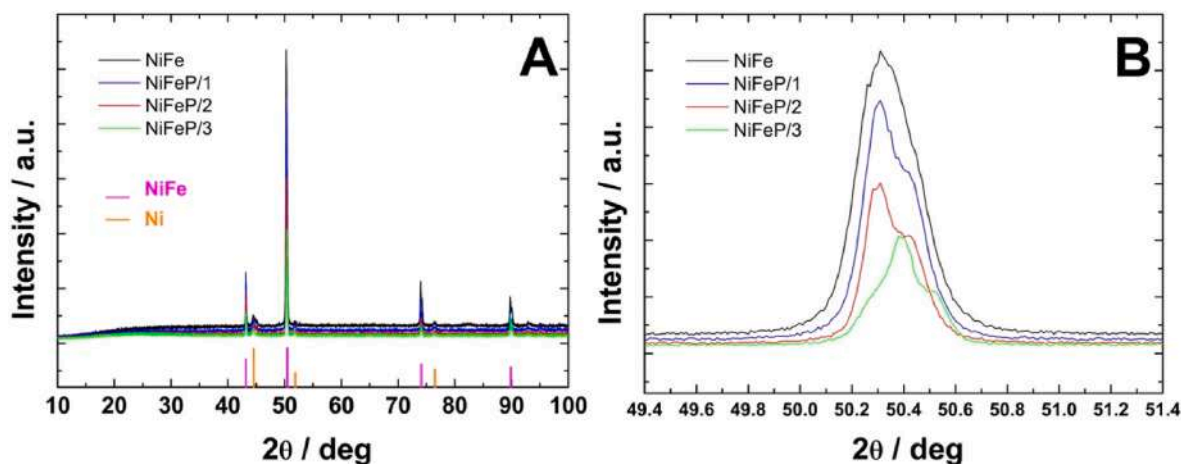
Fig. 5. a) XRD patterns of NiFeP NWs with different phosphorus concentrations. For comparison, the pattern of NiFe NWs was also reported. b) Detail of the main diffraction peak.
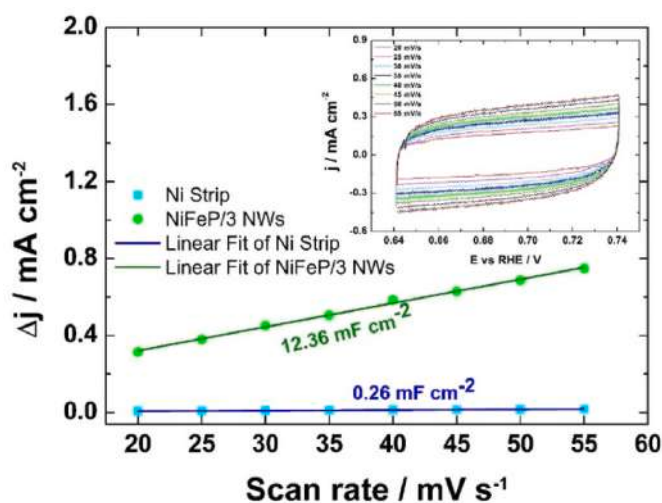

Fig. 6. Specific capacitance of the electrodes evaluated using the double layer capacitance method.

Figure, the effect of the improvement in performance thanks to the presence of P in the alloy can be observed. In particular, for HER, performance increases as the P content increases, while for OER different P concentrations lead to practically the same result. The values of η_{10} (overpotential at 10 mA/cm^2) and η_{100} (overpotential at 100 mA/cm^2) [52] for HER and OER were also measured and reported in Fig. 7C and D.
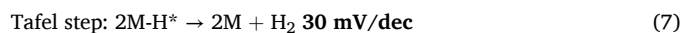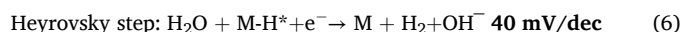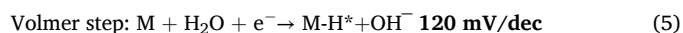
At a current density of 10 mA/cm^2, the η values for NiFeP/3 electrode are −123 mV for HER and 270 mV for OER, respectively, while at 100 mA/cm^2 the η values are −250 mV (for HER) and 360 mV (for OER). These values are better than those measured for the binary NiFe alloy and a planar Ni strip thus, the electrodes obtained herein have good catalytic properties.

The linear range of QSSP curves was fitted, as shown in Fig. 8, with Tafel's equation (equation (4))

$$\eta = a + b \log i \tag{4}$$

where a and b values are an exchange current density and Tafel's curve slope, respectively. The Tafel slope is an intrinsic property of the catalyst that is linked to the kinetically decisive stage of HER and OER processes. A smaller Tafel slope means faster formation of the two gases. Calculated Tafel parameters are listed in Table 2.
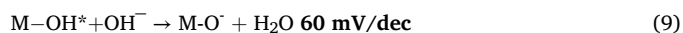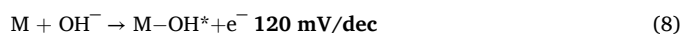
An HER process in alkaline media follows the well-known Volmer-Tafel or Volmer-Heyrovský mechanisms associated with the Tafel slope value [18,25]. In the Volmer step (equation (5)) adsorbed hydrogen forms on a metal surface. This step is followed by an electrochemical desorption (Heyrovsky reaction, equation (6)) or by a chemical desorption (Tafel reaction, equation (7)).

Volmer step: $M + H_2O + e^- \rightarrow M\text{-}H^* + OH^-$ **120 mV/dec** (5)

Heyrovsky step: $H_2O + M\text{-}H^* + e^- \rightarrow M + H_2 + OH^-$ **40 mV/dec** (6)

Tafel step: $2M\text{-}H^* \rightarrow 2M + H_2$ **30 mV/dec** (7)

where M represents the electrode material and M-H* represents the hydrogen adsorbed on the electrode surface.

The Tafel's slope of NiFeP electrodes is lower than that of NiFe electrodes, indicating a faster HER kinetics of the ternary alloy. The best value was obtained for NiFeP/3 electrodes, which have a similar amount of phosphorus to the other alloys, but have the least intense diffraction peaks and, therefore, the least crystalline [31]. The Tafel slope value is between 96 and 88 mV/dec, suggesting that the HER kinetics follows the Volmer-Heyrovsky mechanism.

For NiFeP electrocatalyst, the proposed OER mechanism involves 4 steps (equations (8)–(11)) with the formation of various intermediates [50,53].

$M + OH^- \rightarrow M\text{-}OH^* + e^-$ **120 mV/dec** (8)

$M\text{-}OH^* + OH^- \rightarrow M\text{-}O^- + H_2O$ **60 mV/dec** (9)

$M\text{-}O^- \rightarrow M\text{-}O + e^-$ **45 mV/dec** (10)

$2M\text{-}O \rightarrow 2M + O_2$ **19 mV/dec** (11)

where the symbol * indicates the adsorbed species on the electrode surface. The Tafel slopes of all nanostructured electrodes show a close relationship of approximately 45 mV/dec, indicating that the rate-controlling step is related to M-O formation. The ternary alloy outperforms the binary alloy. In this case, the three alloys obtained have similar performances, independent of the P concentration. The Tafel slope values for both HER and OER are equivalent to or better than similar catalysts containing iron-group elements and phosphorus [25, 36].

The turnover frequency (TOF) is another important parameter linked with the catalytic activity of the electrocatalysts. It can be calculated using equation 12
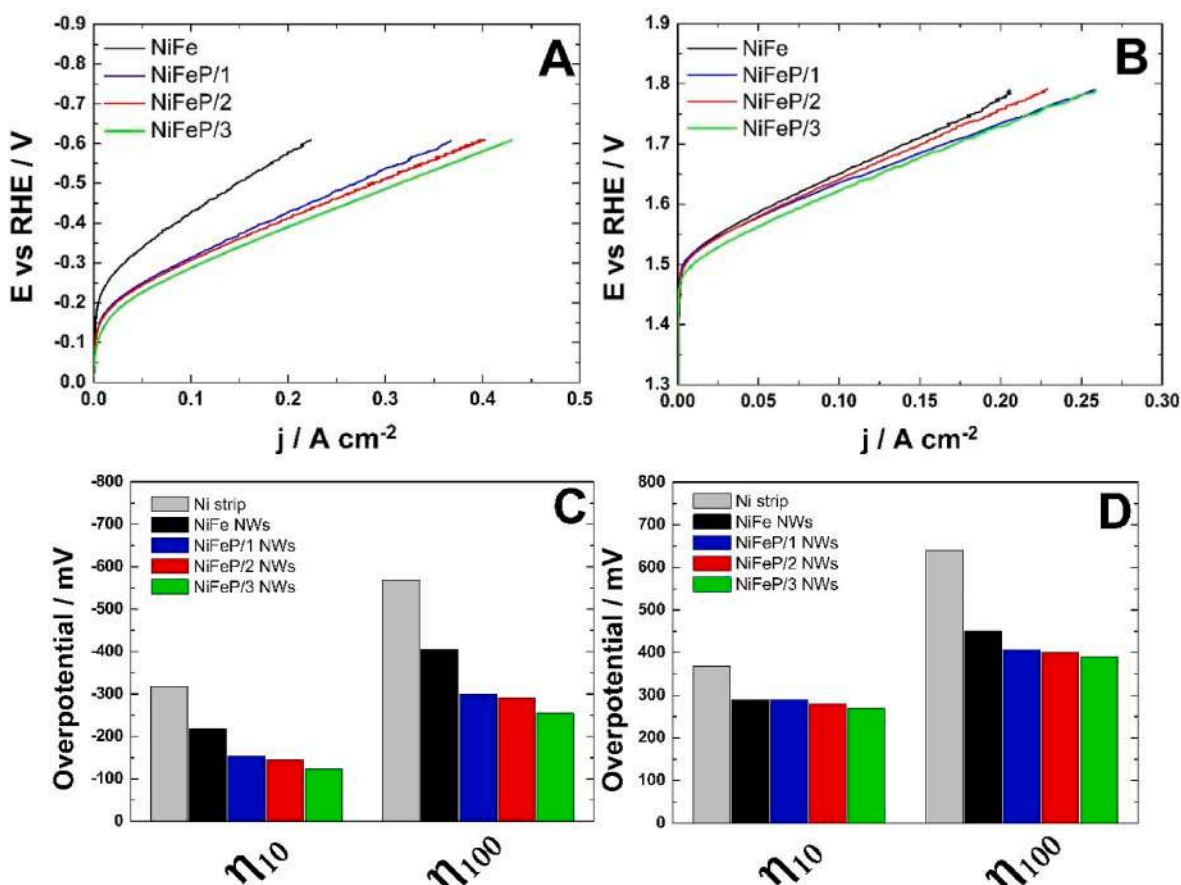
$$TOF = \frac{iA}{xnF} \tag{12}$$

Fig. 7. QSSP for (a) HER and (b) OER at 0.1667 mV s^{-1} in KOH aqueous solution. (c) and (d) values of overpotential at 10 mA/cm^2 and 100 mA/cm^2 for HER and OER, respectively.

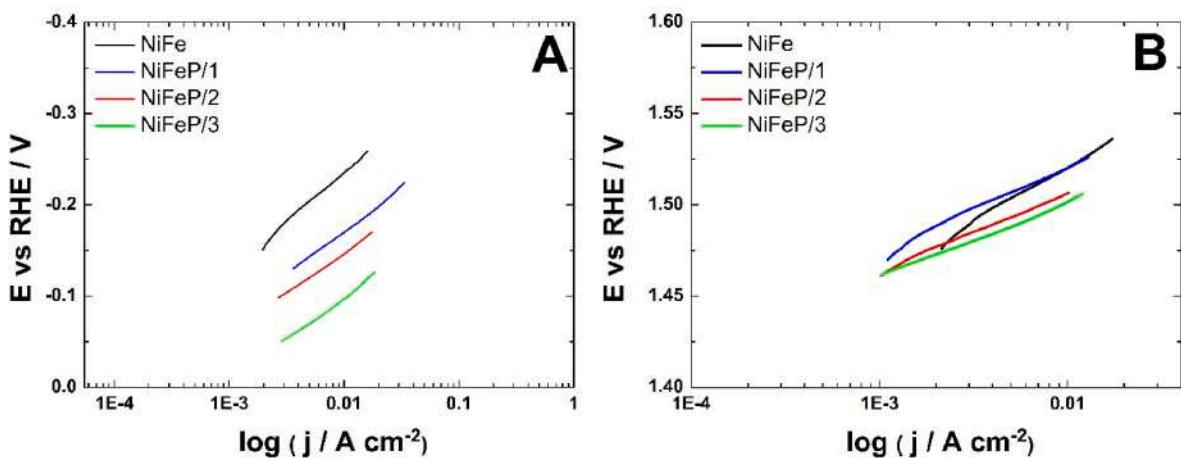**Fig. 8.** Linearity range of QSSP curves for (a) HER and (b) OER.

Table 2
Fitted Tafel's parameters for HER and OER.

Solution	HER			OER		
	a (V)	b (V/dec)	R^2 (%)	a (V)	b (V/dec)	R^2 (%)
NiFe	−0.46	−0.114	99.2	1.62	0.055	99.6
NiFeP/1	−0.36	−0.096	99.74	1.61	0.049	98.7
NiFeP/2	−0.322	−0.089	99.84	1.592	0.043	98.8
NiFeP/3	−0.271	−0.088	99.81	1.581	0.042	99.2

where i is the current density (A/cm^2), A is the geometrical surface area of the electrode, x is the number of transferred electrons for each molecule of gas produced (x = 2 for HER, x = 4 for OER), F is the Faraday constant equal to 96485 C mol^{-1}, n represents the number of the alloy atoms present on the electrode, and it is calculated from the deposited mass of the catalyst. Moreover, it should be noted that not all atoms of a catalyst are equally active and accessible. It is therefore difficult to obtain an accurate TOF value. Nevertheless, this parameter is pertinent and beneficial for the comparison of the performance of analogous catalytic materials [54]. The TOF values were calculated at a

specific overpotential of 400 mv for both reactions and the results were reported in Table 3. The TOF value was compared with that of the Ni planar sheet and the NiFe alloy. The higher TOF values for the NiFe and NiFeP alloys serve to confirm the high accessibility of the active sites present in these nanostructured materials, in comparison to the accessibility of the active sites present in the Ni foil [55]. Furthermore, the elevated TOF value of the NiFeP alloy compared to NiFe confirms its superior catalytic activity.

Multistep chronopotentiometry tests were carried out to investigate the behaviour of the nanostructured electrodes at varying current densities, Fig. 9. Each applied current density (0.01, 0.02, 0.05, 0.1, 0.2, 0.5 A/cm^2) was maintained for 5 min, after which the average value of potential was measured. Fig. 9 displays the average potential for each step.

Multistep chronopotentiometry tests support the previous results. The catalysts consisting of the ternary alloy exhibited superior efficacy than those of the binary alloy. At elevated current density, 0.5 A/cm^2, starting from the binary alloy and transitioning to the optimal ternary alloy, an energy gain of 300 mV and 230 mV was observed for the cathodic and anodic reactions, respectively.

Furthermore, stability is a critical indicator that reflects the long-term ability of the electrocatalyst to catalyze the desired reactions. To study this aspect, we maintained a constant current density of ± 50 mA/cm^2 for 6 h and monitored the potential during this period. In Fig. 10, each point on the graph represents the average potential measured every half an hour. There was a minimal variation in potential from the beginning to the end of the test. NiFeP electrodes exhibited better performance than those attained with NiFe, with NiFeP/3 displaying the most exemplary result. The presence of phosphorus enhanced HER and OER performance, with electrodes containing more phosphorus producing the best results. HER and OER potential decreased from -0.33 to -0.21 V vs. RHE and 1.61 to 1.57 V vs. RHE, respectively, as NiFeP/3 was used instead of NiFe. Although the presence of phosphorus has a more pronounced effect on the cathode side, there are general effects on the ternary alloy of NiFeP. Phosphorus is negatively charged and serves as a proton acceptor, ultimately weakening the bond strength of the positively charged metal to promote hydrogen desorption. Alloys generally exhibit a synergistic effect among their constituent elements, which enhances electron transfer rates, resulting in optimized electrocatalytic activity [56].

To verify the reproducibility of the fabrication method, three different electrodes, obtained using identical deposition parameters, were tested under the same conditions. In particular, galvanostatic step polarization tests (Fig. 11A) and mid-term stability tests (Fig. 11B) were carried out. The small width of the error bars demonstrates the excellent reproducibility of the fabrication method, which, therefore, is suitable for the fabrication of nanostructured electrocatalysts with excellent and stable performance.

To further investigate the durability of the NiFeP/3 electrode, the stability test was repeated for a longer time, 125 h. In Fig. 12, it can be observed that during the 125 h of the test, the performance of the electrodes remains practically constant. This is an interesting result, given that the lifespan of the electrode is closely linked to its electrocatalytic durability. Additionally, NiFeP/3 electrodes were tested in KOH 30 % + 0.5 M NaCl solution to verify the possibility of using these electrodes as bifunctional catalysts for seawater electrolyzers. Fig. 12 shows that the performance of the electrodes remained virtually constant over the 125 h of the test. It is evident that the ternary alloy

outperforms the binary alloy over the long term, and the difference in performance between the NaCl solution and the other is negligible. For OER, it is very important to note that the potential is lower than the hypochlorite standard reduction potential (at pH 14, the value is 1.714 V vs. RHE). Thus, it can be concluded that these electrodes are selective to OER. These results, combined with the simplicity and the low cost of the template electrochemical synthesis (laboratory estimated cost at around 0.2 €/cm^2 for NiFe and 0.22 €/cm^2 for NiFeP/3, lower than commercial Ni foam that is > 2.5 €/cm^2), make the fabrication of these electrodes easily scalable and therefore applicable on a large scale.

To further study the stability of the catalysts, QSSP tests were repeated after the long-term stability test. As can be seen in Fig. 13A and B, the difference between the tests carried out before and after the long-term stability test is very slight. This is a very interesting result because it demonstrates that the NiFeP/3 nanostructured electrodes exhibit good stability.

Electrode stability was also confirmed by an SEM analysis performed on nanostructured electrodes after the long-term stability test was carried out in the KOH + NaCl solution. The images reported in Fig. 14A and B shows that the nanostructure morphology remains essentially unaffected. No collapse of the nanostructures was observed in the entire electrode area, thus, it can be concluded that these nanostructure arrays are stable. The surface of the nanostructures appears to be more wrinkled and, in some parts, is covered by needle-like structures probably attributable to the formation of a thin layer of oxyhydroxide, as confirmed by X-ray Photoelectron Spectroscopy (XPS) analysis below.

The surface of the electrodes was chemically characterized by XPS before and after the long-term stability test of OER in KOH + NaCl, as shown in Fig. 15. High-resolution spectra were collected for samples before and after alkaline treatment in the regions Fe 2p$_{3/2}$, Ni 2p$_{3/2}$, and C 1s (the latter to reference the binding energy scale to adventitious carbon, 284.8 eV). In the Ni 2p$_{3/2}$ region, the green line multiplet (854.9eV, 855.7eV, 857.7 eV, 860.5 eV, 861.5 eV) indicates the Ni(OH)$_2$ species, while the blue line multiplet (852.6 eV, 856.3 eV, 858.7 eV) is indicative of Ni(0). For the Fe 2p$_{3/2}$ region, it is possible to observe a difference between the Fe(III) multiplet (bottom; 710.0 eV, 711.0 eV, 711.9 eV, 713.0 eV, 714.1 eV) and FeOOH (top; 710,3 eV, 711,3 eV, 712,2 eV, 713.3 eV, 714.4 eV). Lastly, the P 2p region shows the disappearance of the phosphide peak (green line) after the stability test. Before the stability test, the surface analysis showed a superficial composition with comparable relative abundances in Ni, Fe, and P (P:Fe: Ni = 1:1.39:1.45), with P showing both as metal phosphide (129.8 eV, 34 %) and phosphate (133.3 eV). Fe 2p$_{3/2}$ and Ni 2p$_{3/2}$ regions were analyzed with peak envelopes, as suggested in Ref. [57]. Fe 2p$_{3/2}$ region appeared to be entirely composed of Fe(III). While it is plausible that Fe (0) is present, the low abundance and the low SNR make it impossible to quantify its presence. On the other hand, the Ni analysis showed the co-presence of metallic Ni (13.6 %) and Ni(OH)$_2$. After the stability test, the observed surface changes are most evident in the surface composition: P:Fe:Ni ratio became 1:8.32:17,69, with phosphide species disappearing from the P 2p region – leaving only phosphate species, with a steep decrease in relative abundance. At the same time, metallic Ni appeared completely oxidized to Ni(OH)$_2$, while Fe(III) appears to have been converted to FeOOH.

3.2. RES-power seawater electrolyzer

To the production of green hydrogen, the water electrolysis system must be coupled with RESs. This coupling can be indirect or direct. In case of indirect coupling, the electrolysis system is powered by the electrical grid, which can distribute the surplus power possibly generated by RESs, potentially also far away from the electrolyzer. For direct coupling, the power used by the electrolyzer is generated by RESs and distributed using a local grid, e.g. a DC microgrid. In the case of direct coupling, the main drawback is related to RESs variability due to weather conditions. This means that without storage elements, the
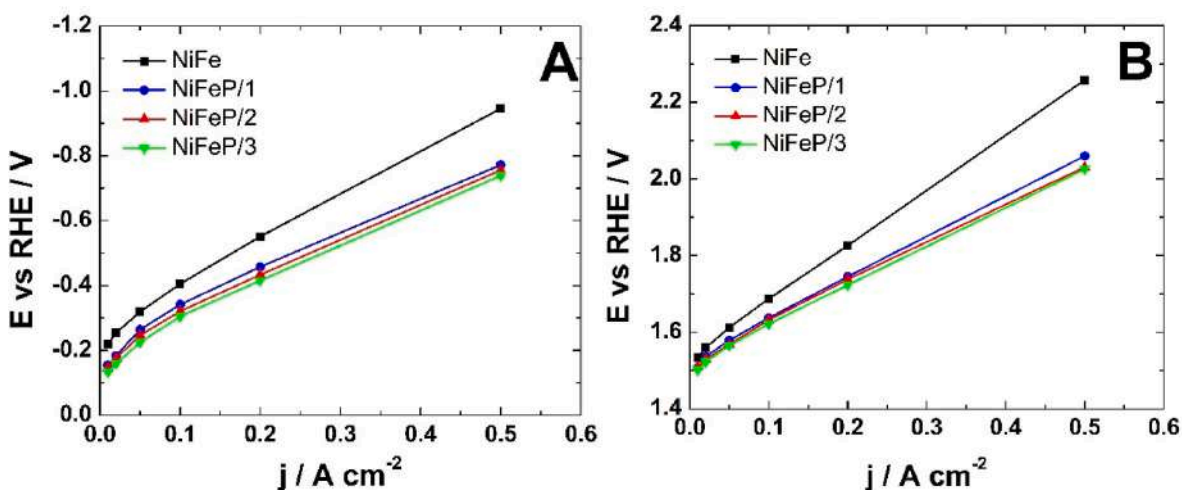
Table 3
TOF values for nanostructured electrodes and planar sheet.

Electrocatalyst	TOF [s-1] HER at η = 400 mV	TOF [s-1] OER at η = 400 mV
Ni Sheet	6.62*10^{-5}	2.5*10^{-5}
NiFe NWs	0.007	0.004
NiFeP NWs	0.0234	0.0059

Fig. 9. Galvanostatic-step polarization for (a) HER and (b) OER.

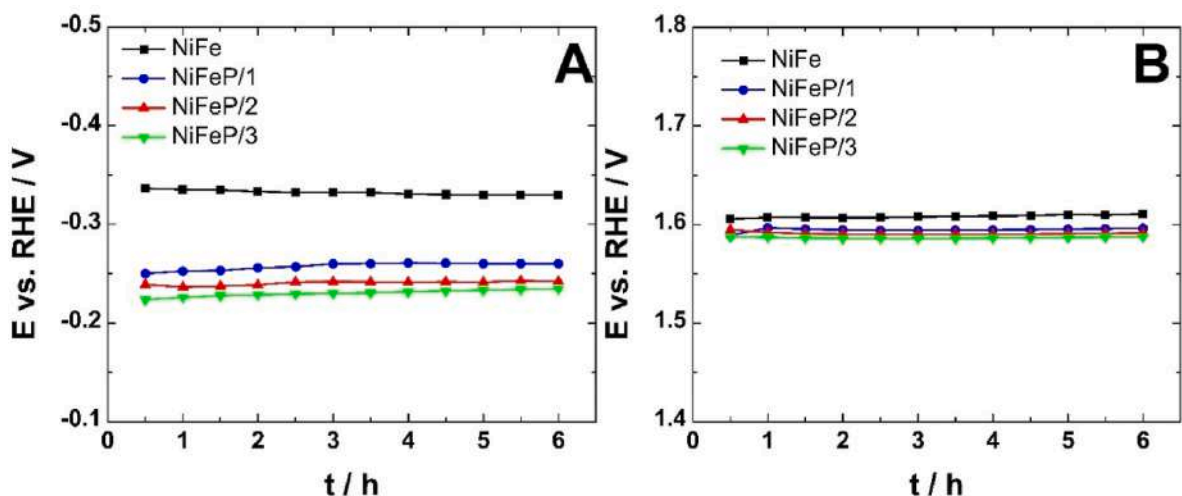**Fig. 10.** Mid-term stability test for 6 h for (a) HER at −50 mA/cm^2 and b) OER at 50 mA/cm^2 in KOH aqueous solution.
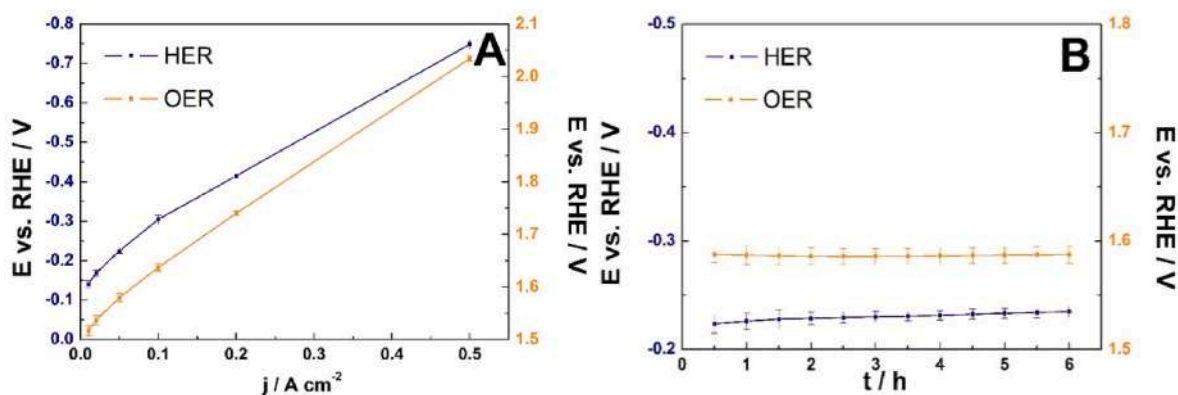

Fig. 11. Galvanostatic-step polarization (a) and (b) mid-term stability test (6 h) for three NiFeP/3 electrodes obtained using identical deposition parameters.

electrolyzer may be subject to variable power supplies and even periods of inactivity that reduce the efficiency of hydrogen production [58] and cause a degradation of the electrocatalysts [59,60]. Thus, it is important to analyse the stability of the electrocatalysts in the case of a direct connection of electrolyzers with RESs. For these reasons, the NiFeP electrodes were tested in a single-cell electrolyzer (using "Simulated SeaWater" as the electrolyte) in long-term stability tests with intermittent power supply, alternating hours of operation at constant current with hours when the electrolyzer was left in open-circuit mode. This is a good way to evaluate the performance of the electrodes under dynamic operation [61]. Since RESs exhibit significant fluctuations, the tests were performed using different discontinuous functioning, simulating
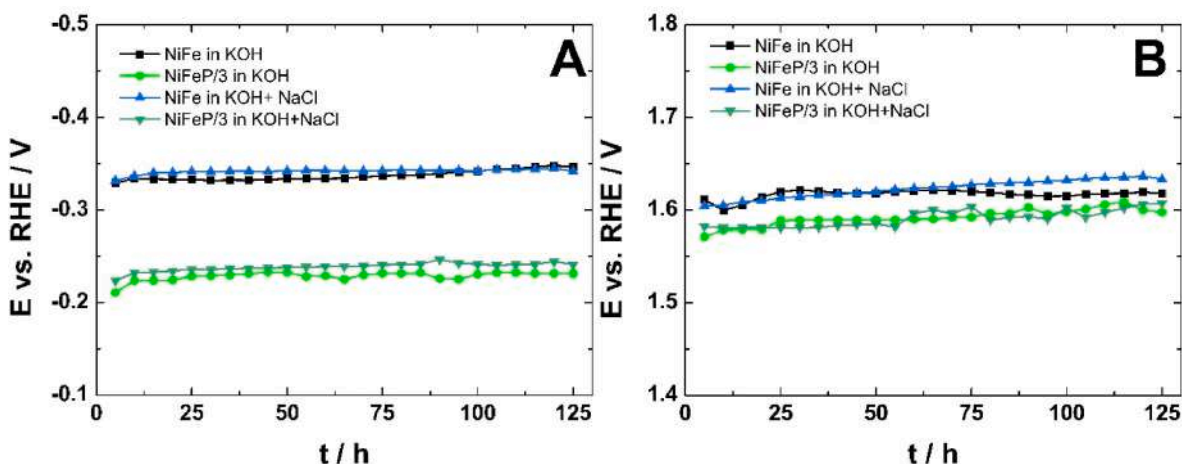
Fig. 12. Long-term stability test for 125 h performed on NiFeP/3 electrodes: (a) HER at -50 mA/cm^2 and (b) OER at 50 mA/cm.^{2}.
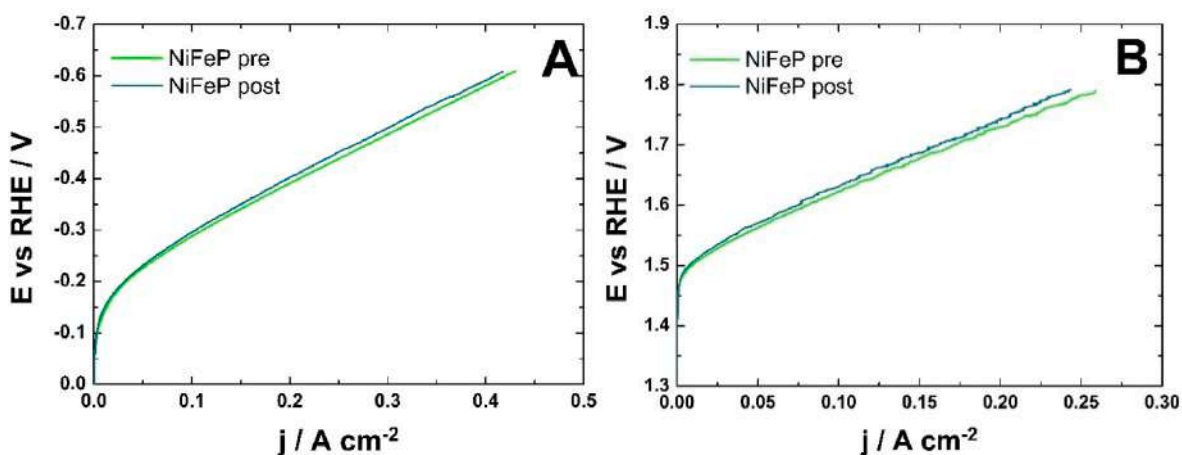

Fig. 13. QSSP test before and after 125 h for (a) HER at -50 mA/cm^2 and (b) OER at 50 mA/cm.^{2}.
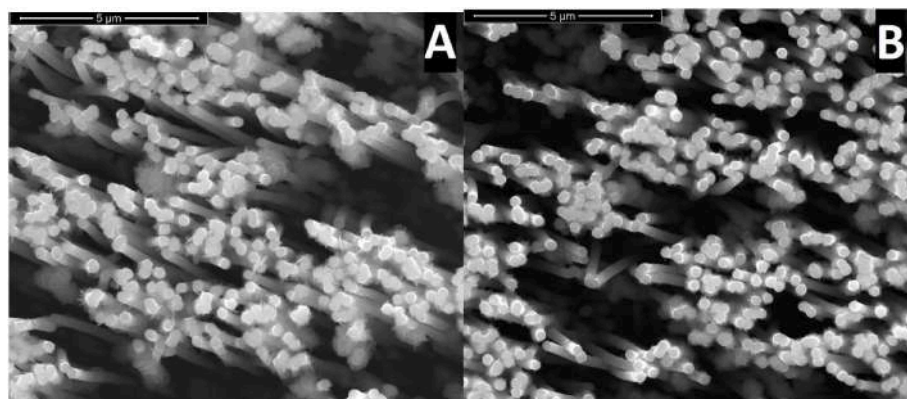

Fig. 14. SEM images of NiFeP/3 NWs electrodes after long-term stability test in KOH + NaCl: A) HER and B) OER.

an operating period of approximately 6 days. In particular, two different profiles were selected.

- A profile corresponding to a day-night photovoltaic cycle: 20 h of operation at ± 50 mA/cm^2 and 4 h at open-circuit potential, Fig. 16A (Solar Power-Seawater Electrolyzer) [62];

- A profile corresponding to a low-wind energy production: 8 h of operation at ± 50 mA/cm^2 and 16 h at open-circuit potential, Fig. 16B (Wind Power- Seawater Electrolyzer) [63].

For both intermittent operations, the curves were obtained by averaging the potential every half hour. In the case of a Solar Power-Seawater Electrolyzer (Fig. 16A), the potential for both HER and OER is almost constant. The potential shifts approximately from -0.213 to
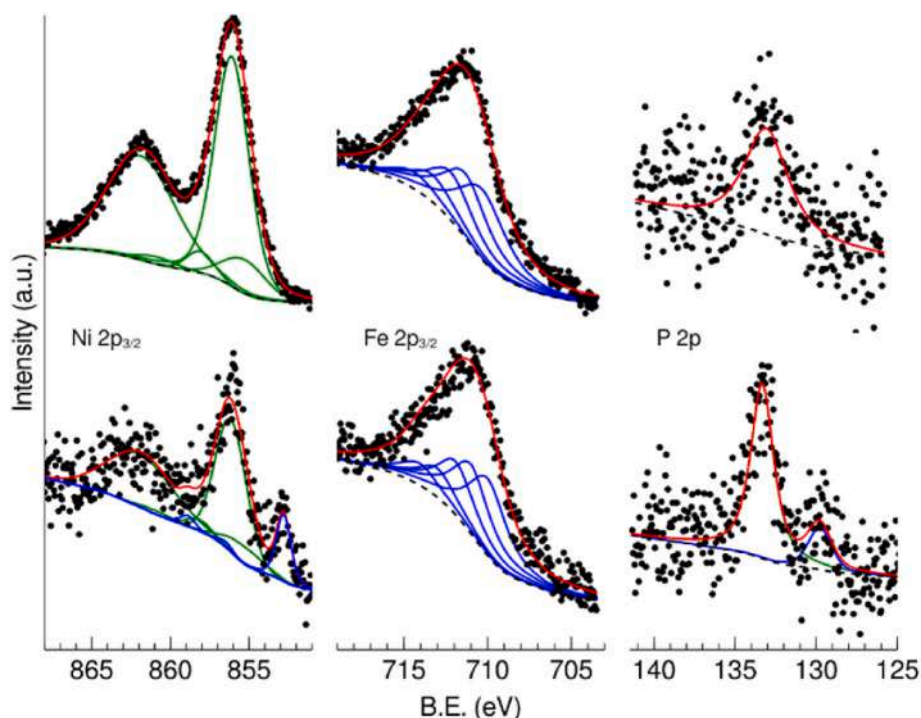
Fig. 15. XPS analysis comparison before (bottom) and after (top) long-term stability test.
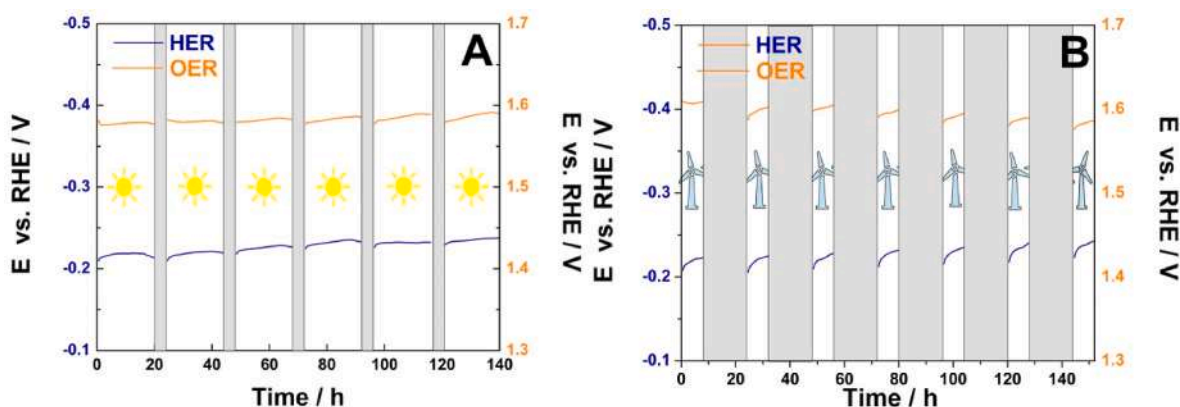

Fig. 16. Intermittent functioning: (A) Solar Power-Seawater Electrolyzer, (B) Wind Power-Seawater Electrolyzer.

−0.235 V for HER and 1.58–1.59 V for OER. For a Wind Power-Seawater Electrolyzer (Fig. 16B), the performance is also good, but especially for the cathodic side, the potential during the 8 h of operation does not reach a stable value, but the values are still comparable to those obtained in the case of solar powering. Interestingly, for both intermittent operations, the potential achieved during the operating hours is comparable to that of continuous operation (Fig. 12), despite the long periods of open circuit, especially in the case of wind energy, which are the phases in which electrocatalysts can suffer the greatest degradation due to dissolution or corrosion phenomena. These results are promising because they suggest good stability of the NiFeP nanostructured electrodes, also in the case of intermittent power supply. Further tests are in progress to simulate operation under further operating variable conditions, such as on a sunny day and a cloudy day.

Although these tests were carried out to investigate the dynamic response of the electrolyzer and verify the stability of the electrocatalysts, they also represent a worst case consisting in a direct coupling between RESs and electrolyzer, without adding other elements. Nevertheless, a more realistic scenario implies the integration of the proposed
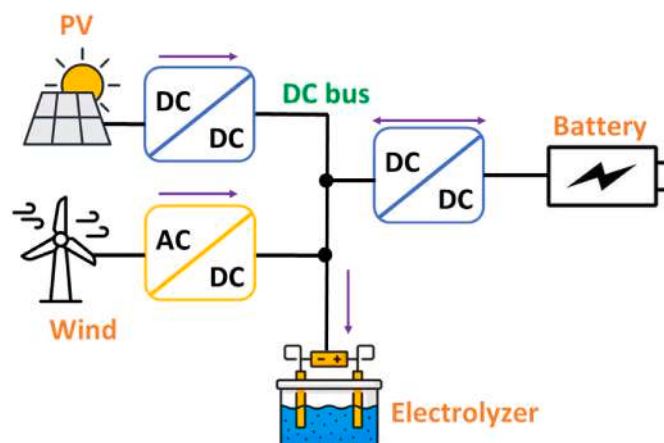

Fig. 17. Power System Architecture connecting RESs, battery and Electrolyzer.

setup with Energy Storage Systems (ESSs) to continuously provide energy to the electrolyzer, whatever the real-time power generated by RESs is. The integration of an ESS is currently underway to facilitate the study of power flow management to the electrolyzer and optimisation of its operation in accordance with the RESs production, using the architecture schematized in Fig. 17. The block diagram regarding a typical power system architecture describing the connection among electrolyzer, RESs and ESSs is shown, where the role of the ESSs is played by a simple battery. Along with RESs, batteries and electrolyzers, the power converters are highlighted as well. The purple arrows represent the possible energy directions. A common DC bus plays the role of interconnector among the different elements. The photovoltaic (PV) plant is connected to the DC bus through a DC-DC converter, whereas the AC power generated by the wind turbine is converted into DC power through an AC-DC converter. The battery is connected to the DC bus through a bidirectional DC-DC converter. When the power arising from the RESs is not sufficient, the battery provides power to the electrolyzer. If there is a surplus of power from RESs, the battery is recharged while the electrolyzer is kept in operation. The RESs-ESSs combination can really guarantee a continuous hydrogen production even during the time windows presenting no power production from RESs, thus leading to less degradation of the cell.

3.3. Laboratory-scale electrolyzer

A laboratory-scale alkaline electrolyzer was constructed using nanostructured electrodes. The NiFeP NWs were assembled into a small electrolytic gap cell AE with an effective electrolysis area of 4 cm^2. The AE was fabricated using poly-methyl methacrylate (PMMA) plates, Fig. 18(A and B), which were specifically designed and shaped using a laser cutter. Two Ni plates serve as current collectors, NiFeP/3 NWs (both acting as anode and cathode) as electrodes, while a Zirfon® foil (Agfa Zirfon Perl UTP 500) was used as the diaphragm. The gasket was made in polytetrafluoroethylene (PTFE) and was shaped with a laser cutter. The electrolyte was pumped through the cells at a constant flow rate with the assistance of peristaltic pumps. For comparison, a laboratory-scale electrolyzer with NiFe NWs electrodes was also fabricated and tested.

Fig. 18C shows the current potential response of the scale-lab electrolyzer. To attain a current density of 10 mA/cm^2, the electrolyzer fabricated with NiFeP NWs electrodes requires a potential of only 1.68 V, smaller than NiFe NWs (1.79 V; inset in Fig. 18C). The electrolyzer was tested for a continuous operation of 6 h at a current density of 50 and 100 mA/cm^2, reaching a potential of 1.91 and 2.01 V, respectively (Fig. 19A). The performances are very stable, given that after a few hours, around 2–3, the potential tends to reach a stable value with an increase during the 6 h of only 20 and 50 mV for a current density of 50

and 100 mA/cm^2, respectively. In addition, multistep chronopotentiometry tests were conducted for additional investigation (Fig. 19B). The laboratory-scale electrolyzer with nanostructured NiFeP demonstrated superior efficacy compared to the binary alloy, confirming the results reported above. The lab-scale electrolyzer is being further optimized to improve the outflow of gas from the surface of the electrodes and, therefore, reduce voltage drops at high current densities.

3.4. Life Cycle Assessment

Life Cycle Assessment (LCA) is a powerful tool for evaluating the potential environmental impacts of a product throughout its lifecycle. The analysis of the entire life cycle detects all hidden environmental impacts, identifying improvement areas and avoiding burden shifting. LCA is characterized by four phases [64].

1. The goal and scope definition includes the aims of the study, the identification of the system boundaries, functional units, allocation procedures, impact categories, and methodologies used for the impact assessment.
2. Life cycle inventory analysis consisting of data collection and calculation to assess the resource consumption, the direct emissions, and the wastes.
3. Life cycle impact assessment, in which, starting from the collected primary and secondary data, the potential environmental impacts are calculated.
4. Life cycle interpretation, in which the results of the previous phase are summarized and commented on to draw conclusions and recommendations.
1. Goal and scope definition

This study is conducted following the international standards UNI EN ISO 14040 [64] and 14044 [65], following an attributional approach. The main goals of the assessment are: to evaluate the energy and environmental impacts of the examined electrode considering three different scenarios; to identify the contribution of each step of the manufacturing stage to the total impacts; to compare the results with a base case of a simple NiFe alloy electrode. The system boundaries are selected following a "from cradle to gate" approach, from raw materials supply to the end of the manufacturing stage. The selected functional unit is 1 cm^2 of electrode. The impact categories chosen for the study are shown in Table 4. The characterization model utilized for the calculation is the EN 15804 + A2 method [66].

2. Life cycle inventory analysis

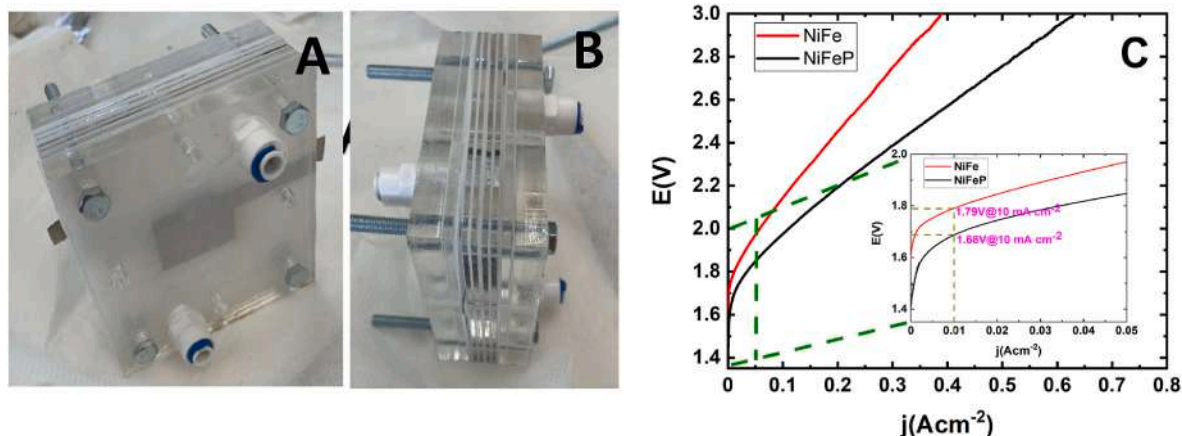The inventory is modelled by examining the manufacturing stage,

Fig. 18. (A and B) Photographs of the laboratory scale alkaline water electrolysis. (C) LSV polarization curves of NiFeP NWs in the AWE cell.
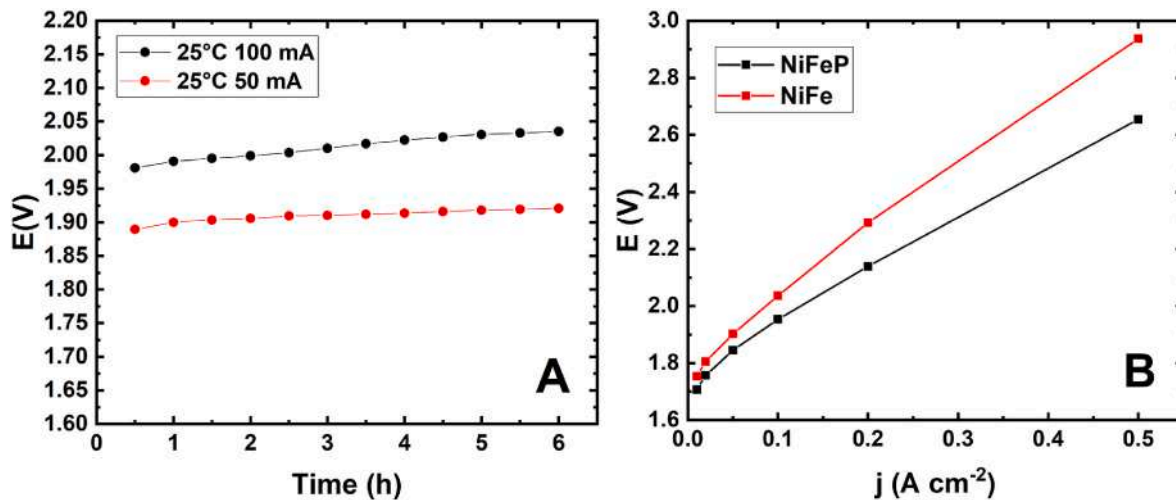
Fig. 19. (a) Mid-term stability test of the laboratory-scale electrolyzer at a current density of 50 and 100 mA/cm^2 for NiFeP NWs. (b) Galvanostatic-step polarization for laboratory-scale electrolyzer with NiFeP and NiFe NWs electrodes.

Table 4
Impact categories selected for the study.

Impact category	Unit of measure
Acidification	mol H$^+_{eq}$
Climate change	kg CO$_{2eq}$
Ecotoxicity, freshwater	CTUe
Eutrophication, freshwater	kg N$_{eq}$
Eutrophication, marine	kg P$_{eq}$
Eutrophication, terrestrial	mol N$_{eq}$
Human toxicity, cancer	CTUh
Human toxicity, non-cancer	CTUh
Ionizing radiation	kBq U-235$_{eq}$
Land use	Pt
Ozone depletion	kg CFC11$_{eq}$
Particulate matter	disease inc.
Photochemical ozone formation	kg NMVOC$_{eq}$
Resource use, fossils	MJ
Resource use, minerals, and metals	kg Sb$_{eq}$
Water use	m$^3_{depriv.}$

Table 6
Electrodeposition.

	Unit of measure	Value
NiSO$_4$	[g/L]	9
NiCl$_2$	[g/L]	1.35
H$_3$BO$_3$	[g/L]	1.35
NaH$_2$PO$_2$	[g/L]	0.6–1.5
FeSO$_4$	[g/L]	0.1
Distilled water	[L]	0.03

Table 7
Trichloromethane (CHCl$_3$) bath.

	Unit of measure	Value
Bath number	[−]	4
Single bath CHCl$_3$	[L]	0.025
Total CHCl$_3$	[L]	0.1

which includes the sputtering process, the electrodeposition, and the etching of polycarbonate templates in trichloromethane.

Primary data on the inputs and output flows are collected at the lab scale for each of the above sub-steps. The inventory analysis is carried out to examine an electrode with a surface of 17.35 cm^2. Three scenarios regarding the composition of sodium hypophosphite (NaH$_2$PO$_2$) are investigated: 0.6 g/L for the first scenario, 0.9 g/L for the second, and 1.2 g/L for the last one. In addition, in the base case, the production process remains unchanged except for the absence of sodium hypophosphite. The primary data collected are reported in Tables 5–7.

All the eco-profiles of the materials and energy sources (secondary data), useful for modelling the supply chains of the materials and energy used, are referred to the Ecoinvent database [67]. Some hypotheses were made to manage the gap of secondary data in the environmental database: the track-etched polycarbonate membrane is substituted by normal polycarbonate; NiCl$_2$ and NaH$_2$PO$_2$ are modelled considering their stoichiometric reactions; distilled water is replaced by deionized

Table 5
Sputtering process.

	Unit of measure	Value
Polycarbonate	[mg]	28.1
Gold	[mg]	1.6
Electrical energy	[Wh]	6.2

water.

3 Life cycle impact assessment and interpretation

The life cycle results referred to the selected functional unit are shown in Table 8. Negligible differences in the results can be observed for the three scenarios: the contribution to the total impacts of the phosphorus precursor used in the electrodeposition step is very low, thus the increasing concentration of this precursor causes a negligible increase in the environmental impacts. Similarly, no significant differences are observed even in the base case without phosphorus, with variation remaining below 1 %, except for land use, where the difference between the base case and the third scenario reaches 3 %.

In addition, a contribution analysis of the electrodeposition process shows that the substances with the highest impact are NiSO$_4$ and NiCl$_2$, with a contribution of about 45 % and 52 %, respectively.

To identify the process in the manufacturing step responsible for the main impacts, a contribution analysis is conducted for the NiFeP/3 (the results are similar for the other scenarios). Fig. 20 shows that the sputtering and the etching in trichloromethane steps cause higher impacts in almost all the impact categories, mainly due to the use of gold and trichloromethane, respectively, while electrodeposition overcomes the other steps only for the "water use" and "acidification" impact categories.

Table 8
Environmental impacts of the selected functional unit for the three scenarios.

Impact category	Unit	Base case	NiFeP/1	NiFeP/2	NiFeP/3
Acidification	mol H_{eq}^+	2.201E-04	2.209E-04	2.213E-04	2.221E-04
Climate change	kg CO_{2eq}	4.101E-02	4.108E-02	4.112E-02	4.119E-02
Ecotoxicity, freshwater	CTUe	5.402E-01	5.422E-01	5.426E-01	6.166E-01
Eutrophication, freshwater	kg N_{eq}	2.342E-05	2.346E-05	2.348E-05	2.353E-05
Eutrophication, marine	kg P_{eq}	2.438E-05	2.443E-05	2.446E-05	2.451E-05
Eutrophication, terrestrial	mol N_{eq}	2.598E-04	2.605E-04	2.608E-04	2.615E-04
Human toxicity, cancer	CTUh	4.117E-10	4.129E-10	4.130E-10	4.131E-10
Human toxicity, non-cancer	CTUh	9.470E-10	9.502E-10	9.518E-10	9.549E-10
Ionizing radiation	kBq U-235_{eq}	4.938E-03	4.941E-03	4.942E-03	4.945E-03
Land use	Pt	9.836E-02	9.959E-02	1.002E-01	1.014E-01
Ozone depletion	kg $CFC11_{eq}$	6.188E-06	6.188E-06	6.188E-06	6.188E-06
Particulate matter	disease inc.	1.049E-09	1.054E-09	1.056E-09	1.061E-09
Photochemical ozone formation	kg $NMVOC_{eq}$	9.396E-05	9.416E-05	9.426E-05	9.446E-05
Resource use, fossils	MJ	3.843E-01	3.847E-01	3.850E-01	3.854E-01
Resource use, minerals, and metals	kg Sb_{eq}	6.874E-06	6.877E-06	6.878E-06	6.880E-06
Water use	$m^3_{depriv.}$	3.340E-02	3.352E-02	3.357E-02	3.369E-02

4. Conclusion

In this work, the behavior of nanostructured NiFeP alloy electrodes, obtained by template electrosynthesis, was studied for water electrolysis at room temperature. The electrodes, which contained approximately 79 % Fe and 6–8 % P, were tested as both cathodes and anodes in 30 % w/w KOH solution. In addition, their suitability for seawater electrolysis was tested in KOH+0.5 M NaCl solution, and the results were compared with those obtained in aqueous KOH solution only. The electrochemical behavior of the electrodes was analyzed using CV, QSSP, and galvanostatic tests. The stability of the nanostructured electrodes was investigated by medium and long-term galvanostatic tests performed at a current density of ± 50 mA/cm^2 for 6 and 125 h, respectively. After the long-term galvanostatic tests, a chemical-physical characterization was performed to identify any potential changes in the morphology and composition of the electrodes. Stability tests were also performed in dynamic conditions typical of direct renewable power supply, obtaining very good performance.

The results indicate that the NiFeP nanostructured electrodes exhibit good catalytic activity for both HER and OER. The presence of NaCl does not appear to affect the stable functioning of the electrode in the short or long term. The catalytic performance in the KOH + NaCl solution is very similar to that of the KOH electrolyte. Furthermore, the electrodes demonstrated mechanical and chemical stability during both medium and long-term gas development. Nanostructured electrodes were also tested for overall water splitting in a lab-scale electrolyzer. Interesting results were obtained, having demonstrated stable performance for 6 h of continuous operation at current densities of 50 and 100 mA/cm^2.

The study also evaluates the environmental impacts of NiFeP electrodes, considering three scenarios varying the phosphorus precursor concentration, through applying LCA methodology. The results show that the increase of phosphorus precursor concentration leads to a negligible increase in the environmental impact, while the contribution analysis indicates that electrodeposition is the process with a lower impact in almost all categories. Likewise, the absence of phosphorus in the base case leads to insignificant variation in impact assessment results. Given the growing importance of these technologies, this study can represent a foundation for further LCA studies on other types of electrodes used in electrolyzers.

CRediT authorship contribution statement

Sonia Carbone: Writing – original draft, Methodology, Investigation. **Roberto Luigi Oliveri:** Writing – original draft, Methodology, Investigation, Data curation. **Bernardo Patella:** Investigation, Data curation. **Giuseppe Aiello:** Formal analysis, Conceptualization. **Michelangelo Scopelliti:** Writing – original draft, Investigation. **Nicola Campagna:** Investigation, Formal analysis. **Filippo Pellitteri:** Writing – original draft, Methodology, Conceptualization. **Rosario Miceli:**
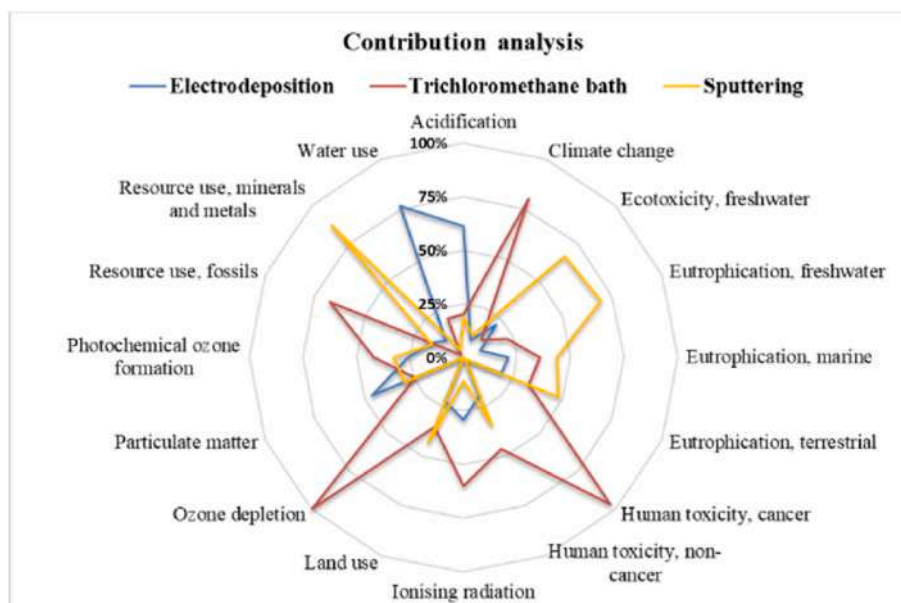
Fig. 20. Contribution analysis of NiFeP/3.

Supervision, Funding acquisition, Conceptualization. **Alberto Affranchi:** Methodology, Investigation, Data curation. **Sonia Longo:** Writing – original draft, Methodology, Formal analysis, Conceptualization. **Maurizio Cellura:** Supervision, Methodology, Funding acquisition, Conceptualization. **Philippe Mandin:** Writing – review & editing, Methodology, Formal analysis, Conceptualization. **Myeongsub Kim:** Writing – review & editing, Supervision, Methodology, Conceptualization. **Rosalinda Inguanta:** Writing – review & editing, Supervision, Funding acquisition, Conceptualization.

Declaration of competing interest

The authors declare the following financial interests/personal relationships which may be considered as potential competing interests: Rosalinda Inguanta reports financial support was provided by University of Palermo. If there are other authors, they declare that they have no known competing financial interests or personal relationships that could have appeared to influence the work reported in this paper.

Acknowledgments

References

[1] M. Zoghi, N. Hosseinzadeh, S. Gharaie, A. Zare, 4E comprehensive comparison and optimization of different renewable power sources for green hydrogen production, Renew. Energy 240 (2025) 122254, https://doi.org/10.1016/j.renene.2024.122254.

[2] F. Yilmaz, M. Ozturk, R. Selbas, Proposal of an advanced hybrid multigeneration plant using solar energy for sustainable hydrogen generation: a thermodynamic and environmental analysis, Renew. Energy (2025) 122621, https://doi.org/10.1016/j.renene.2025.122621.

[3] Y. Wang, G. Dong, J. Yu, C. Qin, Y. Feng, Y. Deng, M. Zhang, In-situ green hydrogen production from offshore wind farms, a prospective review, Renew. Energy 239 (2025) 122099, https://doi.org/10.1016/j.renene.2024.122099.

[4] A.I. Osman, N. Mehta, A.M. Elgarahy, M. Hefny, A. Al-Hinai, A.H. Al-Muhtaseb, D. W. Rooney, Hydrogen production, storage, utilisation and environmental impacts: a review, Environ. Chem. Lett. 20 (2022) 153–188, https://doi.org/10.1007/s10311-021-01322-8.

[5] R.J. Smith, R.G. Bryant, Metal substitutions incarbonic anhydrase: a halide ion probe study, Biochem. Biophys. Res. Commun. 66 (1975) 1281–1286, https://doi.org/10.1016/0006-291x(75)90498-2.

[6] F. Pellitteri, N. Campagna, R. Inguanta, R. Miceli, Application of a multiphase interleaved DC-DC converter for power-to-hydrogen systems, in: 2023 IEEE 17th Int. Conf. Compat. Power Electron. Power Eng. CPE-POWERENG, IEEE, Tallinn, Estonia, 2023, pp. 1–6, https://doi.org/10.1109/CPE-POWERENG58103.2023.10227382.

[7] O. Akdağ, Modeling and economic evaluation of hybrid renewable energy sources for green hydrogen production: a case study for the mediterranean region, Renew. Energy 240 (2025) 122228, https://doi.org/10.1016/j.renene.2024.122228.

[8] S. Xu, H. Zhao, T. Li, J. Liang, S. Lu, G. Chen, S. Gao, A.M. Asiri, Q. Wu, X. Sun, Iron-based phosphides as electrocatalysts for the hydrogen evolution reaction: recent advances and future prospects, J. Mater. Chem. A 8 (2020) 19729–19745, https://doi.org/10.1039/D0TA05628F.

[9] T.S. Munonde, H. Zheng, M.S. Matseke, P.N. Nomngongo, Y. Wang, P. Tsiakaras, A green approach for enhancing the electrocatalytic activity and stability of NiFe2O4/CB nanospheres towards hydrogen production, Renew. Energy 154 (2020) 704–714, https://doi.org/10.1016/j.renene.2020.03.022.

[10] Q. Han, L. Fan, H. Wan, Recent development of metal alloy nanostructures for electrochemical hydrogen generation, Int. J. Electrochem. Sci. 14 (2019) 10549–10559, https://doi.org/10.20964/2019.12.21.

[11] S. Wang, A. Lu, C.-J. Zhong, Hydrogen production from water electrolysis: role of catalysts, Nano Converg 8 (2021) 4, https://doi.org/10.1186/s40580-021-00254-x.

[12] M. Tahir, L. Pan, F. Idrees, X. Zhang, L. Wang, J.-J. Zou, Z.L. Wang, Electrocatalytic oxygen evolution reaction for energy conversion and storage: a comprehensive review, Nano Energy 37 (2017) 136–157, https://doi.org/10.1016/j.nanoen.2017.05.022.

[13] S.V. Chauhan, K.K. Joshi, P.M. Pataniya, P. Sahatiya, G. Bhadu, C.K. Sumesh, Fe2B/MXene@NF electrocatalyst for efficient water splitting and green hydrogen

[14] production at high current densities, Renew. Energy 241 (2025) 122370, https://doi.org/10.1016/j.renene.2025.122370.

[14] M. Rashid, M.K.A. Mesfer, H. Naseem, M. Danish, Hydrogen Production by Water Electrolysis: a Review of Alkaline Water Electrolysis, PEM Water Electrolysis and High Temperature Water Electrolysis, vol. 4 (n.d.) 15.

[15] G. Bender, M. Carmo, T. Smolinka, A. Gago, N. Danilovic, M. Mueller, F. Ganci, A. Fallisch, P. Lettenmeier, K.A. Friedrich, K. Ayers, B. Pivovar, J. Mergel, D. Stolten, Initial approaches in benchmarking and round robin testing for proton exchange membrane water electrolyzers, Int. J. Hydrogen Energy 44 (2019) 9174–9187, https://doi.org/10.1016/j.ijhydene.2019.02.074.

[16] S.W. Sharshir, A. Joseph, M.M. Elsayad, A.A. Tareemi, A.W. Kandeal, M. R. Elkadeem, A review of recent advances in alkaline electrolyzer for green hydrogen production: performance improvement and applications, Int. J. Hydrogen Energy 49 (2024) 458–488, https://doi.org/10.1016/j.ijhydene.2023.08.107.

[17] Y. Li, X. Bao, D. Chen, Z. Wang, N. Dewangan, M. Li, Z. Xu, J. Wang, S. Kawi, Q. Zhong, A minireview on nickel-based heterogeneous electrocatalysts for water splitting, ChemCatChem 11 (2019) 5913–5928, https://doi.org/10.1002/cctc.201901682.

[18] N.A. Khan, G. Rahman, T.M. Nguyen, A.U.H.A. Shah, C.Q. Pham, M.X. Tran, D.L. T. Nguyen, Recent development of nanostructured nickel metal-based electrocatalysts for hydrogen evolution reaction: a review, Top. Catal. 66 (2023) 149–181, https://doi.org/10.1007/s11244-022-01706-2.

[19] B. Hüner, N. Demir, M.F. Kaya, Ni-Pt coating on graphene based 3D printed electrodes for hydrogen evolution reactions in alkaline media, Fuel 331 (2023) 125971, https://doi.org/10.1016/j.fuel.2022.125971.

[20] Y. Zhou, T. Lin, X. Luo, Z. Yan, J. Wu, J. Wang, Y. Shen, Mechanistic study on nickel-molybdenum based electrocatalysts for the hydrogen evolution reaction, J. Catal. 388 (2020) 122–129, https://doi.org/10.1016/j.jcat.2020.05.011.

[21] W.A. Badawy, H. Nady, G.M. Abd El-Hafez, Electrodeposited Zn-Ni alloys as promising catalysts for hydrogen production-Preparation, characterization and electro-catalytic activity, J. Alloys Compd. 699 (2017) 1146–1156, https://doi.org/10.1016/j.jallcom.2016.12.228.

[22] A. Maurya, S. Suman, A. Bhardwaj, L. Mohapatra, A.K. Kushwaha, Substrate dependent electrodeposition of Ni–Co alloy for efficient hydrogen evolution reaction, Electrocatalysis 14 (2023) 68–77, https://doi.org/10.1007/s12678-022-00773-z.

[23] J. Tourneur, C. Lagrost, B. Fabre, Robust and bifunctional electrodeposited NiCoCr ternary alloy for alkaline water electrolysis, Adv. Energy Sustain. Res. (2023) 2300133, https://doi.org/10.1002/aesr.202300133.

[24] J. Mohammed-Ibrahim, A review on NiFe-based electrocatalysts for efficient alkaline oxygen evolution reaction, J. Power Sources 448 (2020) 227375, https://doi.org/10.1016/j.jpowsour.2019.227375.

[25] H.-M. Zhang, J.-J. Wang, Y. Meng, J. Sun, Recent advances in amorphous metal phosphide electrocatalysts for hydrogen evolution reaction, Int. J. Hydrogen Energy 47 (2022) 36084–36097, https://doi.org/10.1016/j.ijhydene.2022.08.184.

[26] D.K. Sam, Y. Cao, Electrocatalytic activities of iron-supported N-doped porous carbon towards the oxygen/hydrogen evolution reaction, Renew. Energy 237 (2024) 121788, https://doi.org/10.1016/j.renene.2024.121788.

[27] M.-I. Jamesh, X. Sun, Recent progress on earth abundant electrocatalysts for oxygen evolution reaction (OER) in alkaline medium to achieve efficient water splitting – a review, J. Power Sources 400 (2018) 31–68, https://doi.org/10.1016/j.jpowsour.2018.07.125.

[28] J. Xu, J. Li, D. Xiong, B. Zhang, Y. Liu, K.-H. Wu, I. Amorim, W. Li, L. Liu, Trends in activity for the oxygen evolution reaction on transition metal (M = Fe, Co, Ni) phosphide pre-catalysts, Chem. Sci. 9 (2018) 3470–3476, https://doi.org/10.1039/C7SC05033J.

[29] M. Ledendecker, S. Krick Calderón, C. Papp, H.-P. Steinrück, M. Antonietti, M. Shalom, The synthesis of nanostructured Ni₅P₄ films and their use as a non-noble bifunctional electrocatalyst for full water splitting, Angew. Chem. Int. Ed. 54 (2015) 12361–12365, https://doi.org/10.1002/anie.201502438.

[30] F. Zhao, X. Mao, X. Zheng, H. Liu, L. Zhu, W. Li, Z. Wang, H. Chen, Roles of the self-reconstruction layer in the catalytic stability of a NiFeP catalyst during the oxygen evolution reaction, J. Mater. Chem. A 11 (2023) 276–286, https://doi.org/10.1039/D2TA06514B.

[31] W. Xu, R. Qiu, X. Mao, X. Yang, B. Peng, Y. Shen, One-step fabrication of amorphous Ni-Fe phosphated alloys as efficient bifunctional electrocatalysts for overall water splitting, J. Non-Cryst. Solids 587 (2022) 121598, https://doi.org/10.1016/j.jnoncrysol.2022.121598.

[32] J. Zhang, K. Hou, Q. Yao, C. Wu, M. Huang, L. Guan, Heterogeneous Ni-Fe-P integrated with nickel foam as an efficient and durable electrocatalyst for water oxidation, Int. J. Hydrogen Energy 44 (2019) 11684–11694, https://doi.org/10.1016/j.ijhydene.2019.03.151.

[33] J.O. Silva, S. Cartagena, J.A. Calderón, Novel electrodeposited NiFeP/Zn bifunctional catalytic coating for alkaline water splitting, Electrochim. Acta 451 (2023) 142299, https://doi.org/10.1016/j.electacta.2023.142299.

[34] P. Liu, J.A. Rodriguez, Catalysts for hydrogen evolution from the [NiFe] hydrogenase to the Ni₂P(001) surface: the importance of ensemble effect, J. Am. Chem. Soc. 127 (2005) 14871–14878, https://doi.org/10.1021/ja0540019.

[35] R. Zhang, X. Wang, S. Yu, T. Wen, X. Zhu, F. Yang, X. Sun, X. Wang, W. Hu, Ternary NiCo₂Pₓ nanowires as pHuniversal electrocatalysts for highly Efficient Hydrogen evolution reaction, Adv. Mater. 29 (2017) 1605502, https://doi.org/10.1002/adma.201605502.

[36] Y. Li, R. Li, D. Wang, H. Xu, F. Meng, D. Dong, J. Jiang, J. Zhang, M. An, P. Yang, A review: target-Oriented transition metal phosphide design and synthesis for

water splitting, Int. J. Hydrogen Energy 46 (2021) 5131–5149, https://doi.org/10.1016/j.ijhydene.2020.11.030.

[37] F. Ganci, S. Lombardo, C. Sunseri, R. Inguanta, Nanostructured electrodes for hydrogen production in alkaline electrolyzer, Renew. Energy 123 (2018) 117–124, https://doi.org/10.1016/j.renene.2018.02.033.

[38] S. Carbone, F. Proietto, F. Bonafede, R.L. Oliveri, B. Patella, F. Ganci, G. Aiello, P. Mandin, M. Kim, M. Scopelliti, R. Inguanta, Behavior of a forest of NiFe nanowires in KOH and NaCl solution for water electrolysis, Electrochim. Acta 467 (2023) 143120, https://doi.org/10.1016/j.electacta.2023.143120.

[39] M. Lai, D.J. Riley, Templated electrosynthesis of nanomaterials and porous structures, J. Colloid Interface Sci. 323 (2008) 203–212, https://doi.org/10.1016/j.jcis.2008.04.054.

[40] B. Buccheri, F. Ganci, B. Patella, G. Aiello, P. Mandin, R. Inguanta, Ni-Fe alloy nanostructured electrodes for water splitting in alkaline electrolyser, Electrochim. Acta 388 (2021) 138588, https://doi.org/10.1016/j.electacta.2021.138588.

[41] F. Ganci, B. Patella, E. Cannata, V. Cusumano, G. Aiello, C. Sunseri, P. Mandin, R. Inguanta, Ni alloy nanowires as high efficiency electrode materials for alkaline electrolysers, Int. J. Hydrogen Energy 46 (2021) 35777–35789, https://doi.org/10.1016/j.ijhydene.2020.11.208.

[42] G. Barati Darband, M. Aliofkhazraei, S. Hyun, S. Shanmugam, Pulse electrodeposition of a superhydrophilic and binder-free ni–fe–p nanostructure as highly active and durable electrocatalyst for both hydrogen and oxygen evolution reactions, ACS Appl. Mater. Interfaces 12 (2020) 53719–53730, https://doi.org/10.1021/acsami.0c13648.

[43] R. Li, Y. Li, P. Yang, D. Wang, H. Xu, B. Wang, F. Meng, J. Zhang, M. An, Electrodeposition: synthesis of advanced transition metal-based catalyst for hydrogen production via electrolysis of water, J. Energy Chem. 57 (2021) 547–566, https://doi.org/10.1016/j.jechem.2020.08.040.

[44] O. Dragos, H. Chiriac, N. Lupu, M. Grigoras, I. Tabakovic, Anomalous codeposition of *fcc* NiFe nanowires with 5–55% Fe and their morphology, crystal structure and magnetic properties, J. Electrochem. Soc. 163 (2016) D83–D94, https://doi.org/10.1149/2.0771603jes.

[45] K. Sridharan, K. Sheppard, Electrodeposition of amorphous iron-nickel-phosphorus alloy coatings, Trans. IMF 72 (1994) 153–158, https://doi.org/10.1080/00202967.1994.11871044.

[46] B. Lafuente, R.T. Downs, H. Yang, N. Stone, 1. The power of databases: the RRUFF project, in: T. Armbruster, R.M. Danisi (Eds.), Highlights Mineral. Crystallogr., DE GRUYTER, 2015, pp. 1–30, https://doi.org/10.1515/9783110417104-003.

[47] Z. Wei, M. Guo, Q. Zhang, Scalable electrodeposition of NiFe-based electrocatalysts with self-evolving multi-vacancies for high-performance industrial water electrolysis, Appl. Catal. B Environ. 322 (2023) 122101, https://doi.org/10.1016/j.apcatb.2022.122101.

[48] Y. Wang, M. Wang, T. Li, Preparation of Fe-Doped Transition Metal Phosphides Using Ionic Liquid as Precursor for Efficient Oxygen Evolution Reaction, (n.d.).

[49] S. Dresp, F. Dionigi, M. Klingenhof, P. Strasser, Direct electrolytic splitting of seawater: opportunities and challenges, ACS Energy Lett. 4 (2019) 933–942, https://doi.org/10.1021/acsenergylett.9b00220.

[50] J. Lian, Y. Wu, H. Zhang, S. Gu, Z. Zeng, X. Ye, One-step synthesis of amorphous ni–fe–p alloy as bifunctional electrocatalyst for overall water splitting in alkaline medium, Int. J. Hydrogen Energy 43 (2018) 12929–12938, https://doi.org/10.1016/j.ijhydene.2018.05.107.

[51] F. Schröper, D. Brüggemann, Y. Mourzina, B. Wolfrum, A. Offenhäusser, D. Mayer, Analyzing the electroactive surface of gold nanopillars by electrochemical methods for electrode miniaturization, Electrochim. Acta 53 (2008) 6265–6272, https://doi.org/10.1016/j.electacta.2008.03.068.

[52] J. Zhu, L. Hu, P. Zhao, L.Y.S. Lee, K.-Y. Wong, Recent advances in electrocatalytic hydrogen evolution using nanoparticles, Chem. Rev. 120 (2020) 851–918, https://doi.org/10.1021/acs.chemrev.9b00248.

[53] Q. Liang, G. Brocks, A. Bieberle-Hütter, Oxygen evolution reaction (OER) mechanism under alkaline and acidic conditions, JPhys Energy 3 (2021) 026001, https://doi.org/10.1088/2515-7655/abdc85.

[54] B. Xiong, L. Chen, J. Shi, Anion-containing noble-metal-free bifunctional electrocatalysts for overall water splitting, ACS Catal. 8 (2018) 3688–3707, https://doi.org/10.1021/acscatal.7b04286.

[55] J. Kibsgaard, I. Chorkendorff, Considerations for the scaling-up of water splitting catalysts, Nat. Energy 4 (2019) 430–433, https://doi.org/10.1038/s41560-019-0407-1.

[56] C. Zhang, Y. Xie, H. Deng, C. Zhang, J.-W. Su, Y. Dong, J. Lin, Ternary nickel iron phosphide supported on nickel foam as a high-efficiency electrocatalyst for overall water splitting, Int. J. Hydrogen Energy 43 (2018) 7299–7306, https://doi.org/10.1016/j.ijhydene.2018.02.157.

[57] M.C. Biesinger, B.P. Payne, A.P. Grosvenor, L.W.M. Lau, A.R. Gerson, R.StC. Smart, Resolving surface chemical states in XPS analysis of first row transition metals, oxides and hydroxides: cr, Mn, Fe, Co and Ni, Appl. Surf. Sci. 257 (2011) 2717–2730, https://doi.org/10.1016/j.apsusc.2010.10.051.

[58] Q. Yang, X. Zhao, Z. Ma, Z. Du, Y. Chen, W. You, J. Yang, F. Gou, M. Mao, L. Bai, T. Meng, X. Song, N. Xuan, C. Tang, Y. Zhou, A. Zhang, J. Xu, K. Yue, Stable photovoltaic-wind hydrogen production with comprehensive energy management strategy and technical economic optimization, Renew. Energy 243 (2025) 122549, https://doi.org/10.1016/j.renene.2025.122549.

[59] A. Sánchez-Squella, R. Flores, R. Burgos, F. Morales, A. Nader, P. Valdivia-Lefort, 99.6% efficiency DC-DC coupling for green hydrogen production using PEM electrolyzer, photovoltaic generation and battery storage operating in an off-grid area, Renew. Energy 237 (2024) 121781, https://doi.org/10.1016/j.renene.2024.121781.

[60] H. Kojima, K. Nagasawa, N. Todoroki, Y. Ito, T. Matsui, R. Nakajima, Influence of renewable energy power fluctuations on water electrolysis for green hydrogen production, Int. J. Hydrogen Energy 48 (2023) 4572–4593, https://doi.org/10.1016/j.ijhydene.2022.11.018.

[61] R.A. Marquez, M. Espinosa, E. Kalokowski, Y.J. Son, K. Kawashima, T.V. Le, C. E. Chukwuneke, C.B. Mullins, A guide to electrocatalyst stability using lab-scale alkaline water electrolyzers, ACS Energy Lett. 9 (2024) 547–555, https://doi.org/10.1021/acsenergylett.3c02758.

[62] E. Amores, J. Rodríguez, C. Carreras, Influence of operation parameters in the modeling of alkaline water electrolyzers for hydrogen production, Int. J. Hydrogen Energy 39 (2014) 13063–13078, https://doi.org/10.1016/j.ijhydene.2014.07.001.

[63] S. Dresp, F. Dionigi, S. Loos, J. Ferreira de Araujo, C. Spöri, M. Gliech, H. Dau, P. Strasser, Direct electrolytic splitting of seawater: activity, selectivity, degradation, and recovery studied from the molecular catalyst structure to the electrolyzer cell level, Adv. Energy Mater. 8 (2018) 1800338, https://doi.org/10.1002/aenm.201800338.

[64] UNI EN ISO 14040, Environmental Management – Life Cycle Assessment –Principles and Framework, 2006 n.d.

[65] UNI EN ISO 14044, Environmental Management – Life Cycle Assessment –Requirements and Guidelines, 2006 n.d.

[66] European Commission – Joint Research Centre, EN 15804 reference package based on EF 3.1 reference package. https://eplca.jrc.ec.europa.eu/LCDN/EN15804.xhtml, 2023 n.d.

[67] G. Wernet, C. Bauer, B. Steubing, J. Reinhard, E. Moreno-Ruiz, B. Weidema, The ecoinvent database version 3 (part I): overview and methodology, Int. J. Life Cycle Assess. 21 (2016) 1218–1230, https://doi.org/10.1007/s11367-016-1087-8.